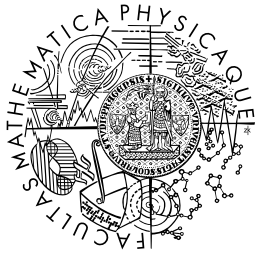

FACULTY
OF MATHEMATICS
AND PHYSICS
Charles University

MASTER THESIS

Ondřej Knopp

Error propagation from the laboratory measurements of electrical conductivity to the Earth's electromagnetic response

Department of Geophysics

Supervisor of the master thesis: Jakub Velímský

Study programme: Mathematical and Computational Modelling in Physics (N0533A110020)

Study branch: FMPMP

Prague 2024

I declare that I carried out this master thesis independently, and only with the cited sources, literature and other professional sources. It has not been used to obtain another or the same degree.

I understand that my work relates to the rights and obligations under the Act No. 121/2000 Sb., the Copyright Act, as amended, in particular the fact that the Charles University has the right to conclude a license agreement on the use of this work as a school work pursuant to Section 60 subsection 1 of the Copyright Act.

In ..... date ....

Author's signature

This research was funded by the Grant Agency of the Czech Republic, project No. 20-07378S, and the Swarm DISC activities, ESA contract No. 4000109587.

Title: Error propagation from the laboratory measurements of electrical conductivity to the Earth's electromagnetic response

Author: Ondřej Knopp

Department: Department of Geophysics

Supervisor: Jakub Velímský, Department of Geophysics

Abstract: Modelling of the electromagnetic response of the Earth has been beneficial for studying its interior. As of late, it is possible to combine this purely electromagnetic modelling with thermodynamic modelling using lab-based measurements of the mantle rock electric conductivity. This coupling of the models can provide insight into the amount of water present in the upper mantle. The experimental lab-based measurements of the mantle rock electric conductivity can introduce unknown amount of error into this process. In this work I will estimate the propagation of such error into the electromagnetic modelling.

Keywords: electrical conductivity electromagnetic induction mantle composition Gibbs energy minimization

Contents

Introduction

The study of the Earth's interior through geophysical methods is an ongoing field of research, providing substantial insights into its structure and composition. In particular, the study of Earth's magnetic response to different internal and external sources, can uncover the Earth's electric conductivity.

Local studies of Earth's magnetic response have been utilized for several decades. The advent of satellite missions, like Swarm, measuring the Earth's magnetic field, have greatly accelerated the study of Earth's deep interior on a global scale.

Not only is the geomagnetic data collection an ongoing project, but also the post-processing of such data into useful dataset is an active field of study. Particular interest for this work have the G019 [Grayver and Olsen, 2019] and MTI [Sabaka et al., 2020] datasets. They applied two different approaches, dedicated and comprehensive inversion, respectively, to extract from the satellite magnetic field measurements the Earth's response to tidal forcing in the Earth's oceans.

Lately, there have been several studies inverting this data into local and global conductivity models of the Earth's upper mantle and transition zone, that range in depth from 100 to 700 km under the sea level. One of the latest works, studying the conductivity of upper mantle, is the one by Šachl et al. [2024].

Another field of active study is interpreting such conductivity models in terms of thermal and chemical composition of Earth's mantle. Such interpretation is not only useful for obtaining more intrinsic physical properties like temperature, but also allows us to cross-reference the results of electromagnetic studies with the results of deep seismic and gravitational sounding.

In this work I will focus on properties of such interpretations. One of my main inspirations is the work of Khan [2016]. This work comprehensively showcases the thermodynamic methods of Connolly [1990, 2005, 2009] coupled with lab-based measurements of mantle rock conductivities to obtain the thermochemical properties of the Earth's upper mantle using electromagnetic data.

Another work motivating this research is the WINTERC-G thermochemical model by Fullea et al. [2021]. This model constructs the thermochemical structure of the Earth, using the previously mentioned thermochemical modelling. The geophysical datasets constraining this model include global seismic sounding, gravity variation measurements and thermal flow data, but exclude the electromagnetic methods.

The WINTERC-G model has been followed up by the WINTERC-e model in Martinec et al. [2021]. It is a synthetic conductivity model constructed from the thermochemical WINTERC-G model using the lab-based mantle rock conductivity data. The viability of this model was validated by comparing its electromagnetic responses to the tidal forcing against the satellite datasets.

The work of Šachl et al. [2024] inverts the tidal magnetic data into the global 3D conductivity of Earths upper mantle. I have contributed to this article by interpreting the resulting conductivity data in terms of water content in the sub-oceanic upper mantle.

My interpretation was achieved using the methods outlined by Khan [2016]. The electric conductivity of upper mantle is very sensitive to the amount of

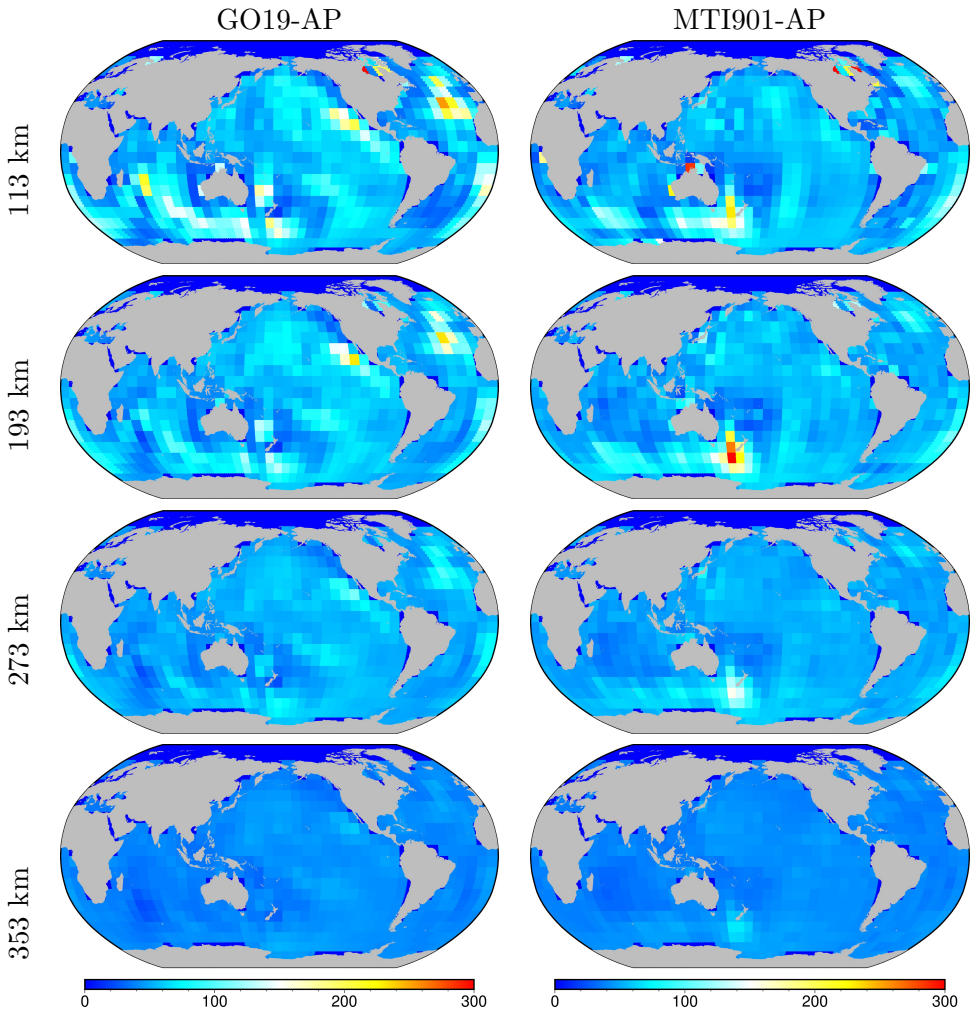

Figure 1: Lower water content estimates in weight fraction [ppm] corresponding to the GO19-AP (left) and MTI (right) datasets.

water present. Due to this I have only interpreted the conductivity in terms of the water content using lab-bases water dependent conductivity measurements and the thermochemical data from the WINTERC-G model.

The results of this interpretation were maps of global suboceanic water content values, illustrated in the Figure 1. This was done for the conductivity models obtained by inversion of the GO19 and the latest MTI datasets by Šachl et al. [2024].

Due to nature of the conductivity interpretation methods used in Šachl et al. [2024], I have only derived the lower and upper estimate of the water content. An illustration of the span between these upper and lower estimates can be better illustrated on a radial profile of the water content shown in the Figure 2.

These upper and lower water content estimates are intrinsic to the water interpretation method and do not reflect the error of such an estimate. The error estimation, for both the upper and lower water content estimate, is exactly what my interpretation of the electric conductivity in Šachl et al. [2024] lacks.

The goal of this work is to study the error of such water content estimations. In the following chapters I will summarize the electromagnetic induction method used in Šachl et al. [2024] to construct the interpreted conductivity models. I

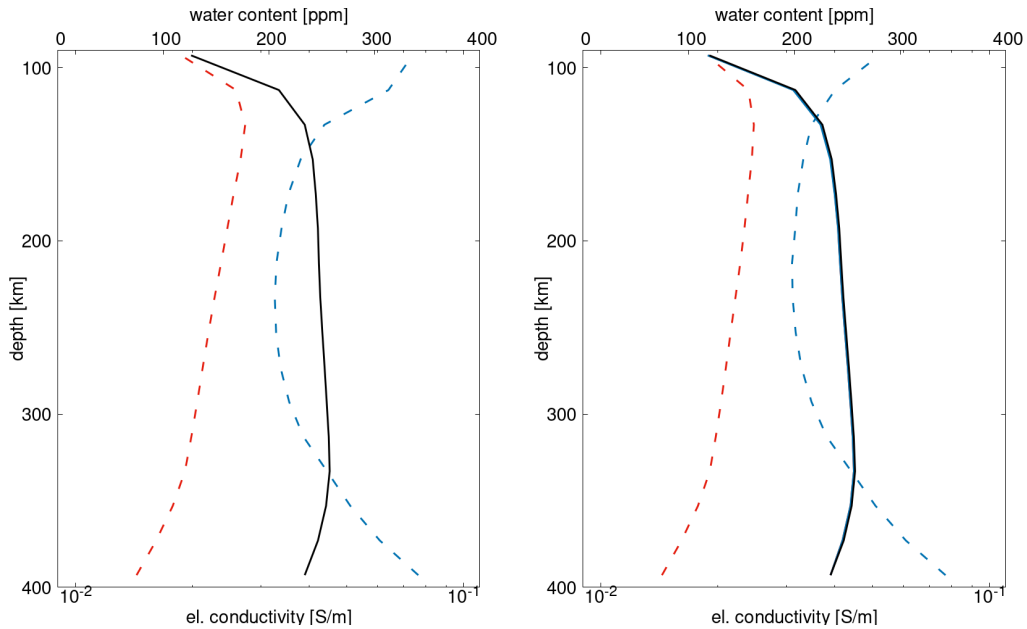

Figure 2: Average suboceanic profile of the lower (red dashed) and upper (blue dashed) water content estimates in weight fraction [ppm] corresponding to the GO19 (left) and MTI (right) conductivity models (black).

will further present the thermodynamic methods for computing the petrological structure of the upper mantle, and the synthesis of lab-based conductivity models.

The lab-based measurements will be considered as the only contributor to the errors of the synthetic conductivity modelling used for water content estimation. I will study the propagation of these errors through synthetic conductivity models and further through the modelling of the electromagnetic response to tidal forcing.

1. Electromagnetic induction, forward problem

This chapter describes the derivation of the electromagnetic induction method used for computing the magnetic response of the Earth to tidally induced currents. This model, used in Šachl et al. [2024], is based on Martinec [1999] and Velímský and Martinec [2005].

1.1 Basic derivation

When modelling the electromagnetic induction (EMI) response of the Earth we first define the modelled variables. The variables at play are the magnetic induction $\mathbf{B}(\mathbf{r},t)$, the magnetic intensity $\mathbf{H}(\mathbf{r},t)$, the electric intensity $\mathbf{E}(\mathbf{r},t)$, the electric induction $\mathbf{D}(\mathbf{r},t)$, the free electric current density $\mathbf{j}_f(\mathbf{r},t)$ and the free static electric charge $\rho_f(\mathbf{r},t)$. These variables are governed by the Maxwell equations in the form

$$\begin{aligned} \nabla\cdot\mathbf{D}=\rho_f,\ \nabla\times\mathbf{E}=\frac{\partial\mathbf{B}}{\partial t},\\ \nabla\cdot B=0,\ \nabla\times\mathbf{H}=\mathbf{j}_f+\frac{\partial\mathbf{D}}{\partial t}. \end{aligned} \tag{1.1}$$

The Maxwell equations must be complemented by so-called material relations binding the variables together. For an isotropic linear medium these are

$$\begin{aligned} \mathbf{D}=\epsilon_0\mathbf{E},\ \mathbf{B}=\mu_0\mathbf{H},\\ \rho_e=\rho_f,\ \mathbf{j}_f=\mathbf{j}=\sigma\mathbf{E}+\sigma\mathbf{u}\times\mathbf{B}, \end{aligned} \tag{1.2}$$

where ϵ_0 is the electric permittivity of vacuum, μ_0 is the magnetic permeability of vacuum, $\sigma(\mathbf{r})$ is the electric conductivity, $\mathbf{j}(\mathbf{r},t)$ is the total current, $\rho_e(\mathbf{r})$ is the total static charge and $\mathbf{u}$ is the velocity of a conductive continuum. The last material relation encodes the Ohm's law and the Lorentz magnetic force, acting on the charge carriers in the direction perpendicular to their movement and the magnetic field.

Assuming zero static charge, the material relations reduce the number of free variables to only two, $\mathbf{B}$ and $\mathbf{E}$. The magnetic field $\mathbf{B}$ and the electric field $\mathbf{E}$ are modelled inside the Earth defined as a perfect sphere G with radius $a\approx 6371\,\mathrm{km}$ with center at $\mathbf{r}=0$. In this case the Maxwell equations take the form

$$\begin{aligned} \nabla\times\mathbf{E}=-\frac{\partial\mathbf{B}}{\partial t},\ \nabla\cdot\mathbf{E}=0,\\ \nabla\times\mathbf{B}=\mu_0\sigma\left(\mathbf{E}+\mathbf{u}\times\mathbf{B}\right)+\mu_0\epsilon_0\frac{\partial\mathbf{E}}{\partial t},\nabla\cdot\mathbf{B}=0. \end{aligned} \tag{1.3}$$

Under the assumption, that the displacement current $\epsilon_0\partial\mathbf{E}/\partial t$ in negligible compared to the electric currents present, we obtain so called magnetoquasistatic approximation of Maxwell's equations

$$\begin{aligned} \nabla\times\mathbf{E}=-\frac{\partial\mathbf{B}}{\partial t},\ \nabla\cdot\mathbf{E}=0,\\ \nabla\times\mathbf{B}=\mu_0\sigma\left(\mathbf{E}+\mathbf{u}\times\mathbf{B}\right),\nabla\cdot\mathbf{B}=0. \end{aligned} \tag{1.4}$$

The goal is to model the magnetic response of a conductive Earth to the tidal forcing in the Earth's oceans. In this case the electrically conductive oceanic seawater is moving in the presence of the magnetic field. This means, that the velocity $\mathbf{u}$ is almost everywhere zero, except for the uppermost layers of G, where the oceans are present.

The total geomagnetic field can be separated into the main magnetic field of the Earth $\mathbf{B}_M$, generated by dynamo action in the Earth's outer core, and the magnetic time variations $\mathbf{B}_t$, so $\mathbf{B} = \mathbf{B}_M(\mathbf{r}) + \mathbf{B}_t(\mathbf{r}, t)$. On the modelled time-scales the field $\mathbf{B}_M$ is time independent. The time-dependent variations $\mathbf{B}_t$ are in this case generated by the tidal forcing and do not include other external sources, like the ones originated in the magnetosphere and ionosphere. These must be treated separately and subtracted from observed geomagnetic field in the process of extraction of tidal signals. The absolute values of the main magnetic field are assumed to be orders of magnitude larger than the time variations, meaning that the current can be approximated as

$$\mathbf{j}_{\text{total}} = \sigma\mathbf{E} + \sigma\mathbf{u} \times \mathbf{B}_M. \tag{1.5}$$

Further I will denote $\mathbf{B}(\mathbf{r}, t)$ as only the tidal magnetic field. The two term in the equation above can be labeled as $\mathbf{j} + \mathbf{j}_{\text{imp}}$, where $\mathbf{j}_{\text{imp}}$ is the imposed current density by the tidal forcing. Moreover, the total current can be rewritten in the terms of electric field only, if we denote the $\mathbf{j}_{\text{imp}} = \sigma\mathbf{E}_{\text{imp}}$.

Altogether this results in the relevant set of equations

$$\begin{aligned} \nabla \times \mathbf{E} = -\frac{\partial \mathbf{B}}{\partial t}, \nabla \cdot \mathbf{E} = 0, \\ \nabla \times \mathbf{B} = \mu_0\sigma(\mathbf{E} + \mathbf{E}_{\text{imp}}), \nabla \cdot \mathbf{B} = 0. \end{aligned} \tag{1.6}$$

Oceanic tidal flows are periodic phenomena, dominated by semi-diurnal and diurnal modes, although non-linear transient tides also exist [Einšpigel and Martinec, 2017]. The tidal patterns can vary on annual time scales, but for purposes of EMI modelling it is assumed that oceanic velocity is strictly periodic, meaning

$$\mathbf{u}(\mathbf{r}, t) = \mathbf{u}(\mathbf{r})e^{i\omega t}. \tag{1.7}$$

There are several tidal constituents, but the largest one is the principal lunar semi-diurnal tide M2. The period of this constituent is not exactly 12 hours, but approximately 12.41 h, due to additional rotation of the Moon. The associated angular frequency is $\omega = 1.41 \cdot 10^{-4}\, s^{-1}$. Due to this periodicity of the ocean tides, the imposed electrical field is also periodic, meaning

$$\mathbf{E}_{\text{imp}}(\mathbf{r}, t) = \mathbf{E}_{(imp)}(\mathbf{r})e^{i\omega t}. \tag{1.8}$$

Due to linear nature of the equations 1.6 it is reasonable to restrict the solution only to a periodic form, meaning

$$\mathbf{B} = \mathbf{B}(\mathbf{r})e^{i\omega t},\ \mathbf{E} = \mathbf{E}(\mathbf{r})e^{i\omega t}. \tag{1.9}$$

From now on I will represent all the time dependent variables $\mathbf{u}, \mathbf{B}, \mathbf{E}, \mathbf{E}_{\text{imp}}$, using their complex amplitudes.

Using this prescribed periodicity, the equations (1.6) can be rewritten as

$$\begin{aligned} \nabla \times \mathbf{E} = -i\omega\mathbf{B}, \nabla \cdot \mathbf{E} = 0, \\ \nabla \times \mathbf{B} = \mu_0\sigma(\mathbf{E} + \mathbf{E}_{\text{imp}}), \nabla \cdot \mathbf{B} = 0. \end{aligned} \tag{1.10}$$

By substituting the unknown electric field $\mathbf{E}$ in to the other equations we reduce the system into only two equation for $\mathbf{B}$:

$$\nabla \times (\rho\nabla \times \mathbf{B}) + i\omega\mu_0\mathbf{B} = \mu_0\nabla \times \mathbf{E}_{\text{imp}}, \tag{1.11}$$

$$\nabla \cdot \mathbf{B} = 0, \tag{1.12}$$

here $\rho(\mathbf{r}) = 1/\sigma(\mathbf{r})$ denotes the electric resistivity of the Earth.

To impose the boundary conditions for a complete strong formulation of the boundary value problem, it is necessary to first explore the properties of the magnetic field outside the conductive Earth. The atmosphere surrounding Earth is considered to be an isolator, meaning $\sigma(\mathbf{r}) = 0$, with no electric currents, $\mathbf{j} = 0$. In this case the equations (1.10) are reduced to

$$\nabla \times \mathbf{B} = 0, \nabla \cdot \mathbf{B} = 0. \tag{1.13}$$

$\nabla \times \mathbf{B} = 0$ implies that the magnetic field is conservative and that it can be parametrized using a single scalar potential $U(\mathbf{r})$. Substituting the magnetic field by the potential in the divergence equation (1.13) yields the equation for U

$$\nabla \cdot (\nabla U) = 0. \tag{1.14}$$

This is a simple Laplace equation. Let's assume the equation is valid everywhere in $\mathbb{R}^3 \setminus G$. Every continuous solution for such a problem can be expressed in spherical coordinates as

$$U(\mathbf{r}) = U(r, \vartheta, \varphi) = a\sum_{j=1}^{\infty}\sum_{m=-j}^{j}\left[G_{jm}^{(e)}\left(\frac{r}{a}\right)^j + G_{jm}^{(i)}\left(\frac{a}{r}\right)^{j+1}\right]Y_{jm}(\vartheta, \varphi), \tag{1.15}$$

where Y_{jm} are fully normalized complex spherical harmonics(SH), defined as

$$Y_{jm}(\vartheta, \varphi) = \sqrt{\frac{(2l+1)}{4\pi}\frac{(l-m!)}{(l+m)!}}P_j^m(\cos\vartheta)e^{im\varphi}, \tag{1.16}$$

where P_j^m are the associated Legendre polynomials, ϑ is colatitude, and φ is longitude.

The variables $G_{jm}^{(e)}$ and $G_{jm}^{(i)}$ are coefficients of so-called external and internal fields. The external terms in equation 1.15 rise with the growing r, meaning they originate outside the Earth, while the internal terms increase as r decreases, meaning they originate inside the Earth.

Demanding that for $r \to \infty$ the magnetic potential vanishes, implies the absence of external fields, meaning the coefficients $G_{jm}^{(e)} = 0$ for all degrees j and orders m.

The magnetic field in the insulating atmosphere given by this potential can be rewritten as

$$\begin{aligned}\mathbf{B}^{(f)} = &-\sum_{j=1}^{\infty}\sum_{m=-j}^{j}\mathbf{S}_{jm}^{(-1)}(\vartheta,\varphi)\left(jG_{jm}^{(e)}\left(\frac{r}{a}\right)^{j-1}-(j+1)G_{jm}^{(i)}\left(\frac{a}{r}\right)^{j+2}\right)\\ &-\sum_{j=1}^{\infty}\sum_{m=-j}^{j}\mathbf{S}_{jm}^{(1)}(\vartheta,\varphi)\left(G_{jm}^{(e)}\left(\frac{r}{a}\right)^{j-1}+G_{jm}^{(i)}\left(\frac{a}{r}\right)^{j+2}\right),\end{aligned} \tag{1.17}$$

where $\mathbf{S}_{jm}^{(\lambda)}$ are the vector spherical harmonics defined as

$$\begin{aligned}\mathbf{S}_{jm}^{(-1)}(\vartheta,\varphi) &= Y_{jm}(\vartheta,\varphi)\mathbf{e}_r,\\ \mathbf{S}_{jm}^{(0)}(\vartheta,\varphi) &= \frac{\partial Y_{jm}}{\partial\vartheta}\mathbf{e}_\varphi-\frac{1}{\sin(\vartheta)}\frac{\partial Y_{jm}}{\partial\vartheta}\mathbf{e}_\vartheta,\\ \mathbf{S}_{jm}^{(1)}(\vartheta,\varphi) &= \frac{\partial Y_{jm}}{\partial\vartheta}\mathbf{e}_\vartheta+\frac{1}{\sin(\vartheta)}\frac{\partial Y_{jm}}{\partial\vartheta}\mathbf{e}_\varphi,\end{aligned} \tag{1.18}$$

where $\mathbf{e}_r$, $\mathbf{e}_\vartheta$, $\mathbf{e}_\varphi$ are unit vectors in the respective spherical coordinates and $\mathbf{B}^{(f)}$ denotes the free-space solution valid outside G.

Now the boundary condition of the EMI problem in G can be set, by enforcing continuity of magnetic field across the conductor-insulator boundary ∂G. The solution inside the Earth can also be expanded using the vector harmonics basis as

$$\mathbf{B}(r,\vartheta,\varphi)=\sum_{j=1}^{\infty}\sum_{m=-j}^{j}\sum_{\lambda=-1}^{1}B_{jm}^{(\lambda)}(r)\mathbf{S}_{jm}^{(\lambda)}(\vartheta,\varphi). \tag{1.19}$$

It is important to point out that the basis $\mathbf{S}_{jm}^{(\lambda)}$ is orthogonal in the $L_2(\Omega)$ norm, where Ω denotes the surface of a unit sphere. Hence, the coefficients of $B_{jm}^{(\lambda)}(r)$ can be obtained as

$$B_{jm}^{(\lambda)}(r)=\left(\delta_{\lambda,-1}+\frac{\delta_{\lambda,0}+\delta_{\lambda,1}}{j(j+1)}\right)\int_\Omega\mathbf{B}(r,\vartheta,\varphi)\cdot\mathbf{S}_{jm}^{(\lambda)}(\vartheta,\varphi)\mathrm{d}\Omega, \tag{1.20}$$

where $\mathrm{d}\Omega$ is a surface element of the unit sphere surface and the term preceding the integral is one over norm of $\mathbf{S}_{jm}^{(\lambda)}$.

The continuity condition $\mathbf{B}(a,\vartheta,\varphi)=\mathbf{B}^{(f)}(a,\vartheta,\varphi)$ implies

$$\begin{aligned}B_{jm}^{(0)}(a) &= 0,\\ B_{jm}^{(-1)}(a) &= -jG_{jm}^{(e)}+(j+1)G_{jm}^{(i)},\\ B_{jm}^{(1)}(a) &= -G_{jm}^{(e)}-G_{jm}^{(i)}.\end{aligned} \tag{1.21}$$

Assuming the coefficients of the external field $G_{jm}^{(e)}$ to be zero and the coefficients of $G_{jm}^{(i)}$ to be unknown, results in two boundary value conditions,

$$\begin{aligned}B_{jm}^{(0)}(a) &= 0,\\ B_{jm}^{(-1)}(a)+(j+1)B_{jm}^{(1)}(a) &= 0.\end{aligned} \tag{1.22}$$

As Velímský and Martinec [2005] mention, such a boundary value condition is necessarily linked to the decomposition of $\mathbf{B}$ into vector spherical harmonics and cannot be expressed as a simple Dirichlet or Neumann boundary condition.

This concludes the definition of a strong formulation of the BPV problem defined as

$$\nabla \times (\rho \nabla \times \mathbf{B}(\mathbf{r})) + i\omega\mu_0 \mathbf{B}(\mathbf{r}) = \mu_0 \nabla \times \mathbf{E}_{\text{imp}}(\mathbf{r}),\ \forall \mathbf{r} \in G, \tag{1.23}$$

$$\nabla \cdot B(\mathbf{r}) = 0,\ \forall \mathbf{r} \in G, \tag{1.24}$$

$$B_{jm}^{(0)}(a) = 0,\ \forall j, m, \tag{1.25}$$

$$B_{jm}^{(-1)}(a) + (j+1) B_{jm}^{(1)}(a) = 0,\ \forall j, m, \tag{1.26}$$

where the magnetic field is a continuous complex vector function $\mathbf{B} : G \to \mathbb{C}^3$ in G, and $B_{jm}^{(\lambda)}(r)$ are complex continuous function in $[0, a] \to \mathbb{C}$ representing the coefficients of the decomposition of $\mathbf{B}$ into vector spherical harmonics. Furthermore, $\mathbf{E}_{\text{imp}}$ is also a complex vector function in G. Lastly $\rho(\mathbf{r})$ is a time-independent positive real continuous function on G.

1.2 Weak formulation

Let's define a solution space $W = W_2^1(G)^3 \times L_2(G)$, where $W_2^1(G)^3$ denotes the Sobolev space of complex vector functions $G \to \mathbb{C}^3$ and $L_2(G)$ denotes the complex Lebesgue space. Let's further define a testing space $V = W_2^1(G)_0^3 \times L_2(G)$, such that for $(\mathbf{B}, \Lambda) \in V$ the tangential components of $\mathbf{B}$ to ∂G are zero on ∂G. Now the weak formulation of the problem is defined as follows. Let the μ_0, ω be constant, real and positive. Let $\rho \in L_2(G)$ be real and positive function and let $\mathbf{E}_{\text{imp}} \in W$. Find $(\mathbf{B}, \Lambda) \in W$ such that

$$i\mu_0\omega(\delta\mathbf{B}, \mathbf{B})_{L_2^3(G)} + a(\delta\mathbf{B}, \mathbf{B}) + b(\delta\mathbf{B}, \delta\Lambda, \mathbf{B}, \Lambda) = F(\delta\mathbf{B}), \forall (\delta\mathbf{B}, \delta\Lambda) \in V, \tag{1.27}$$

$$\int_{\partial G} \mathbf{B} \cdot \mathbf{S}_{jm}^{(0)} \mathrm{d}S = 0,\ \forall j, m \tag{1.28}$$

and

$$\int_{\partial G} \mathbf{B} \cdot \mathbf{S}_{jm}^{(-1)} + (j+1)\mathbf{B} \cdot \mathbf{S}_{jm}^{(1)} \mathrm{d}S = 0,\ \forall j, m. \tag{1.29}$$

Here the form $a(\delta\mathbf{B}, \mathbf{B})$ is defined as

$$a(\delta\mathbf{B}, \mathbf{B}) = \int_G \rho(\nabla \times \delta\mathbf{B}) \cdot \overline{(\nabla \times \mathbf{B})}\, \mathrm{d}V, \tag{1.30}$$

and the form $b(\delta\mathbf{B}, \delta\lambda, \mathbf{B}, \lambda)$ is defined as

$$b(\delta\mathbf{B}, \delta\Lambda, \mathbf{B}, \Lambda) = \int_G \overline{\Lambda}(\nabla \cdot \delta\mathbf{B}) + \int_G \delta\Lambda \cdot \overline{\nabla \cdot \mathbf{B}}\, \mathrm{d}V. \tag{1.31}$$

This form encodes the equation $\nabla \cdot \mathbf{B} = 0$ using Lagrange multipliers Λ.

The linear form $F(\delta\mathbf{B})$ is defined by the internal forcing as

$$F(\delta\mathbf{B}) = \int_G \nabla \times \overline{\mathbf{E}_{\text{imp}}} \cdot \delta\mathbf{B}\, \mathrm{d}V = \int_G \overline{\mathbf{E}_{\text{imp}}} \cdot \nabla \times \delta\mathbf{B}\, \mathrm{d}V. \tag{1.32}$$

1.3 Discretization

1.3.1 Lateral discretization

The weak formulation can be approximated by selecting the testing functions and solution from a subset of a solution space, where all the complex functions can be expressed as

$$\begin{aligned}\mathbf{B}(\mathbf{r}) &= \sum_{j=1}^{j_{\max}} \sum_{m=-j}^{j} \sum_{\lambda=-1}^{1} B_{jm}^{(\lambda)}(r)\mathbf{S}_{jm}^{(\lambda)}, \\ \Lambda(\mathbf{r}) &= \sum_{j=1}^{j_{\max}} \sum_{m=-j}^{j} \Lambda_{jm}(r) Y_{jm},\end{aligned} \tag{1.33}$$

where $B_{jm}^{(\lambda)}(r) \in W_2^1([0,a])$ and $\Lambda_{jm}(r) \in L_2([0,a])$ for all $j \leq j_{\max}$ and $m = -j, \ldots, j$, where $j_{\max}$ is SH cutoff.

Let's express the divergence and rotation of $\mathbf{B}(\mathbf{r})$ using the functions $D(\mathbf{r})$ and $\mathbf{R}(\mathbf{r})$

$$D = \nabla \cdot \mathbf{B}(\mathbf{r}) = \sum_{j=1}^{j_{\max}} \sum_{m=-j}^{j} D_{jm} Y_{jm}, \tag{1.34}$$

$$\mathbf{R} = \nabla \times \mathbf{B}(\mathbf{r}) = \sum_{j=1}^{j_{\max}} \sum_{m=-j}^{j} \sum_{\lambda=-1}^{1} R_{jm}^{(\lambda)} \mathbf{S}_{jm}^{(\lambda)}. \tag{1.35}$$

It can be shown from the properties of spherical harmonic functions, that the functions D_{jm} are $R_{jm}^{(\lambda)}$ are equal to

$$D_{jm} = \left(\frac{d}{dr} - \frac{2}{r}\right) B_{jm}^{(-1)} - j(j+1)\frac{1}{r} B_{jm}^{(1)}, \tag{1.36}$$

$$R_{jm}^{(-1)} = -j(j-1)\frac{1}{r} B_{jm}^{(0)}, \tag{1.37}$$

$$R_{jm}^{(1)} = -\left(\frac{d}{dr} - \frac{1}{r}\right) B_{jm}^{(0)}, \tag{1.38}$$

$$R_{jm}^{(0)} = -\frac{1}{r} B_{jm}^{(-1)} + \left(\frac{d}{dr} - \frac{1}{r}\right) B_{jm}^{(1)}. \tag{1.39}$$

Let $a_l(\delta\mathbf{B}, \mathbf{B})$ and $b_l(\delta\mathbf{B}, \delta\Lambda, \mathbf{B}, \Lambda)$ be the corresponding linear forms for such approximated spaces, expressed in the lateral SH basis. Martinec [1999] shows that

$$a_l(\delta\mathbf{B}, \mathbf{B}) = \sum_{j=1}^{j_{\max}} \sum_{m=-j}^{j} \sum_{\lambda=-1}^{1} \int_0^a \delta R_{jm}^{(\lambda)}(r; \overline{\mathbf{R}})_{jm}^{(\lambda)} r^2 \mathrm{d}r, \tag{1.40}$$

where $(r; \overline{\mathbf{R}})$ is defined as

$$(r; \overline{\mathbf{R}})_{jm}^{(\lambda)} = \int_\Omega \rho(r, \Omega) \sum_{j_1=1}^{j_{\max}} \sum_{m_1=-j_1}^{j_1} \sum_{\lambda_1=-1}^{1} \overline{R}_{j_1 m_1}^{(\lambda_1)}(r) \overline{\mathbf{S}}_{j_1 m_1}^{(\lambda_1)}(\Omega) \cdot \mathbf{S}_{jm}^{(\lambda)}(\Omega) \mathrm{d}\Omega. \tag{1.41}$$

It is important to point out, that if the resistivity has no lateral variations, this term is reduced to $\overline{R}_{jm}^{(\lambda)}(r)$ due to orthogonality of $S_{jm}^{(\lambda)}$ basis in the $L_2^3(G)$ norm. The operator $b_l(\delta\mathbf{B}, \delta\Lambda, \mathbf{B}, \Lambda)$ can be expressed as

$$\begin{aligned} b_l(\delta\mathbf{B}, \delta\lambda, \mathbf{B}, \lambda) = &\sum_{j=1}^{j_{\max}} \sum_{m=-j}^{j} \int_0^a \delta\Lambda_{jm} \overline{D}_{jm} r^2 \mathrm{d}r \\ &+ \sum_{j=1}^{j_{\max}} \sum_{m=-j}^{j} \int_0^a \overline{\Lambda_{jm}} \delta D_{jm} r^2 \mathrm{d}r. \end{aligned} \tag{1.42}$$

The leading term of the $L_2(G)^3$ scalar product can be written as

$$(\delta\mathbf{B}, \mathbf{B})_{L_2^3(G)} = \sum_{j=1}^{j_{\max}} \sum_{m=-j}^{j} \sum_{\lambda=-1}^{1} \int_0^a \delta B_{jm}^{(\lambda)} \overline{B}_{jm}^{(\lambda)} r^2 \mathrm{d}r. \tag{1.43}$$

Finally, the right-hand side can be rewritten as

$$\sum_{j=1}^{j_{\max}} \sum_{m=-j}^{j} \sum_{\lambda=-1}^{1} \int_0^a \mathbf{E}_{\mathrm{imp},jm}^{(\lambda)} \delta R_{jm}^{(\lambda)} r^2 \mathrm{d}r. \tag{1.44}$$

1.3.2 Radial discretization

We can subdivide the interval $[0, a]$ into n subintervals $[r_k, r_{k+1}]$, such that $0 = r_0 < r_1 < \ldots < r_n = a$. We use a simple finite element discretization of the $W_2^1([0, a])$ and $L_2^1([0, a])$ spaces using set of basis functions

$$\psi_k(r) = \begin{cases} \frac{r - r_{k-1}}{h_k}, & r \in [r_{k-1}, r_k], \\ \frac{r_k - r}{h_{k+1}}, & r \in [r_k, r_{k+1}], \\ 0, & \text{elsewhere}, \end{cases} \tag{1.45}$$

for discretizing $W_2^1([0, a])$, defined for $k = 0, 1, \ldots, n$ and

$$\eta_k(r) = \begin{cases} 1, & r \in [r_k, r_{k+1}], \\ 0, & \text{elsewhere}, \end{cases} \tag{1.46}$$

to discretize $L_2^1([0, a])$, defined for $k = 0, 1, \ldots, n-1$ and, $h_k = r_k - r_{k-1}$.

The magnetic field coefficients $B_{jm}^{(\lambda)}$ and the Lagrange multiplier coefficients Λ_{jm} can be represented in these bases as

$$B_{jm}^{(\lambda)}(r) = \sum_{k=0}^{n} B_{jm}^{(\lambda),k} \psi_k(r), \tag{1.47}$$

$$\Lambda_{jm}(r) = \sum_{k=0}^{n-1} \Lambda_{jm}^{k} \eta_k(r). \tag{1.48}$$

The same can be done for the electric conductivity σ and the internal forcing $\mathbf{E}_{\mathrm{imp}}$

$$\sigma(\vartheta, \varphi, r) = \sum_{k=0}^{n} \sigma^k(\vartheta, \varphi) \eta_k(r), \tag{1.49}$$

$$\mathbf{E}^{(\lambda)}_{\mathrm{imp},jm} = \sum_{k=0}^{n} \mathbf{E}^{(\lambda),k}_{\mathrm{imp,jm}} \eta_k(r). \tag{1.50}$$

The final set of variables can be represented by the vectors

$$\mathbf{b} = (B^{(\lambda),k}_{jm})_{k=0,1,\ldots,n;j=1,\ldots,j_{\max};m=-j,\ldots,j;\lambda=-1,0,1} \in \mathbb{C}^{3\cdot(n+1)\cdot(j_{\max}+2)j_{\max}}, \tag{1.51}$$

$$\mathbf{v} = (\lambda^{k}_{jm})_{k=0,1,\ldots,n-1;j=1,\ldots,j_{\max},m=-j,\ldots,j} \in \mathbb{C}^{n\cdot(j_{\max}+2)j_{\max}}. \tag{1.52}$$

I will not delve into the full Galerkin approximation of the equations 1.27. The discretization is described in Velímský and Martinec [2005] for the whole equation except for the Lagrange constituent. The discretization of the Lagrange multiplier part can be found in Martinec [1999]. The most important observation about matrices derived from the Galerkin method, is the case where the resistivity $\rho(\mathbf{r}) = \rho(r)$ is strictly radially dependent. As shown in Martinec [1999], the term $(r;\overline{\mathbf{R}})^{l}_{jm}$ collapses into ρR^{l}_{jm}. In this case otherwise dense matrix of the Galerkin approximation takes the form of a band matrix.

The solution of the discretized model above can be obtained using elmgFD code by Velímský et al. [2018], which employs effective LAPACK subroutines for factorization and solution of the band matrices stemming from the 1-D problem. Although the existence and uniqueness of a solution of the weak formulation is not shown, the code representing the Galerkin discretization was successfully benchmarked against several other codes based on different approaches (integral equations, finite differences). This validation was presented in Velímský et al. [2018].

1.4 Internal forcing

The right-hand side of the linear system, depends on the tidal flows and the main magnetic field. The tidal flows are for this purpose represented by a 2D vector $\mathbf{U}(\vartheta,\varphi)$ representing the vertically integrated velocity of the ocean currents. Such a vector has zero radial part. Under the assumption, that the velocity is constant throughout the entire water column, the point-wise velocity can be written as

$$\mathbf{u}(r,\vartheta,\varphi) = \begin{cases} \mathbf{U}(\vartheta,\varphi)/b(\vartheta,\varphi), & r > a - b(\vartheta,\varphi), \\ 0, & \text{otherwise} \end{cases}, \tag{1.53}$$

here $b(\vartheta,\varphi)$ is the bathymetry, depth of the ocean at the coordinates (ϑ,φ).

The main field $\mathbf{B}_M(r,\vartheta,\varphi)$, is represented in spherical harmonics, where the coefficients taken from the 13th generation International Geomagnetic Reference Field IGRF-13 [Alken et al., 2021]. This model of the Earth's magnetic field also expresses its time dependence using first derivatives of the coefficients. However, this secular variation of the main field has negligible impact on the tidal signals, and $\mathbf{B}_M$ is expressed for a fixed epoch 2015.0. The bathymetry and the vertically integrated oceanic velocity is taken from the model TPXO9 by Egbert and Erofeeva [2002] for the M2 tidal flow patterns. To obtain the internal forcing $\mathbf{E}_{\mathrm{imp}}$ described in vector spherical harmonics, the term $\mathbf{u}\times\mathbf{B}_M$ is computed on a Gaussian grid for each layer containing ocean and then projected into the vector spherical harmonics.

2. Thermodynamic modelling of mantle rocks

In this chapter I present the thermodynamic method for computing the mineral structure of the Earth's mantle. Such method utilizes the Gibbs energy minimization, and its discretization as implemented in the Perple_X software. I use the formalism and the approach presented by Connolly [1990, 2005, 2009], the author of Perple_X, with some minor changes to the notation.

The next section of this chapter, presenting the theory of the Gibbs energy method, has been mostly copied verbatim from my Bachelor thesis [Knopp, 2021], due to identity of the topic at hand.

2.1 Gibbs energy minimization

For a time-independent model of the Earth's mantle, it is possible to characterize a small enough region of the mantle only by its chemical composition, pressure and temperature. In order to determine other physical properties such as density, viscosity, thermal and electrical conductivity, heat capacity and microscopic arrangement of its components, it is sufficient to apply the Gibbs energy minimization approach. The Gibbs energy $G(P, T, \mathbf{X})$ in thermodynamic sense depends only on the temperature T, the pressure P, and the composition vector $\mathbf{X} = (X_1, X_2, \ldots, X_d)$. The composition vector consists of the individual component fractions in the mixture with d components,

$$X_i = N_i/N, \tag{2.1}$$

where N_i is the number of particles for the i-th component, and

$$N = \sum_{i=1}^{d} N_i. \tag{2.2}$$

Obviously, $\mathbf{X}$ lives in the unit d-simplex

$$P_d = \left\{ \mathbf{X} \in [0,1]^d, \sum_{i=1}^{d} X_i = 1 \right\}. \tag{2.3}$$

For fixed (P, T) conditions and a given total chemical composition, $\mathbf{X}^0$, the system can contain up to s coexisting phases in a thermodynamic equilibrium. Each of these phases has a distinct composition vector $\mathbf{X}^j$ and corresponding concentration in the system ψ^j. It must hold, that

$$1 = \sum_{j=1}^{s} \psi^j, \tag{2.4}$$

$$\mathbf{X}^0 = \sum_{j=1}^{s} \psi^j \mathbf{X}^j. \tag{2.5}$$

The complete knowledge of the Gibbs energy $G_{P,T}(\mathbf{X}) \equiv G(P,T,\mathbf{X})$ yields the number of phases s, the concentrations ψ^j, and the compositions $\mathbf{X}^j$ of the coexisting phases by minimizing the function

$$g\left(s, \{\psi^j, \mathbf{X}^j\}_{j=1}^s\right) = \sum_{j=1}^{s} \psi^j G_{P,T}(\mathbf{X}^j), \tag{2.6}$$

subjected to constraints (2.4, 2.5). It can be shown, that the optimal value of this sum lies on the convex hull of the function $G_{P,T}(\mathbf{X})$, where the total composition vector $\mathbf{X}^0$ is projected on the convex hull as shown in the Figure 2.1. In other words,

$$\sum_{j=1}^{s} \psi^j G_{P,T}(\mathbf{X}^j) \leq G_{P,T}(\mathbf{X}^0). \tag{2.7}$$

Furthermore the composition vectors of the coexisting phases can be found at the intersections of the function $G_{P,T}(\mathbf{X})$ with its own convex hull. Then the concentrations ψ^j can be viewed as barycentric coordinates of the point $(g, \mathbf{X}^0)$ in a s-simplex with the vertices $\{(G_{P,T}(\mathbf{X}^j), \mathbf{X}^j)\}_{j=1}^s$.

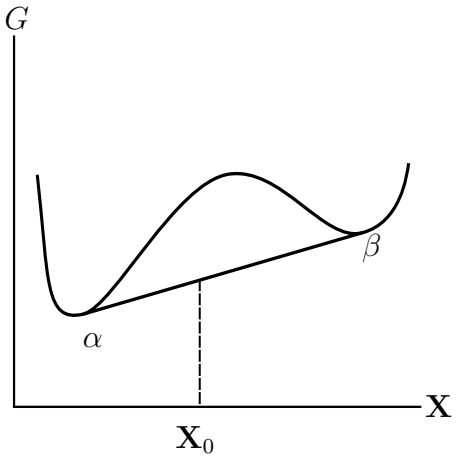

Figure 2.1: A simplified scheme of a two-phase, two-component system $\mathbf{X} = (x, 1-x)$. For a fixed temperature and pressure, there are two minima of the Gibbs energy $G_{PT}(\mathbf{X})$ representing the two phases α and β. For a fixed composition $\mathbf{X}^0 = (x^0, 1-x^0)$, the Gibbs energy $G_{PT}(\mathbf{X}^0)$ is not optimal. Considering presence of heterogeneities in the system, the optimal Gibbs energy lies on the convex hull of the function $G_{PT}(\mathbf{X})$.

The number s itself can be determined according to the Gibbs phase rule. It states, that $s = d + 2 - f$, where f is the number of degrees of freedom on the (P,T) phase diagram. For most (P,T) conditions it holds, that $f = 2$. However, when phase transitions occur due to the temperature or the pressure change, the number of degrees of freedom can also reach the value 0 or 1.

Note that s is the maximal number of coexisting phases. For example, if $\mathbf{X}^j = \mathbf{X}^0$ for a particular phase j, then $\psi^j = 1$ and $\psi^i = 0$, $\forall i \neq j$. This concept is generalized also for those $\mathbf{X}^0$ positioned on edges or faces of the s-simplex considered above.

This exact analytical approach has its obvious downsides. First, one has to know the complete function $G(P,T,\mathbf{X})$ in order to construct its convex hull

for each P and T. Another complication arises from the identification of the intersection points. Nevertheless, this framework provides an efficient tool to explain the presence of different phases and their coexistence. It also serves as a guide for construction of discrete phase transition approximations.

One of the simplest approximations is a model with finite number of chemically pre-identified phases. Let there be S known possible phases in the model. Each phase has a defined chemical composition $\mathbf{X}^j$, and a known Gibbs energy function $\bar{G}^j(P,T)$. The total composition of the system is $\mathbf{X}^0$ and we aim to constrain the concentrations of the individual phases $\bar{\psi}^j$. Again it must hold, that

$$1 = \sum_{j=1}^{S} \bar{\psi}^j, \tag{2.8}$$

$$\mathbf{X}^0 = \sum_{j=1}^{S} \bar{\psi}^j \mathbf{X}^j. \tag{2.9}$$

The concentrations $\bar{\psi}^j$ complying with these conditions, must minimize the expression

$$\bar{g}_{P,T}(\{\bar{\psi}^j\}_{j=1}^{S}) = \sum_{j=1}^{S} \bar{\psi}^j \bar{G}^j(P,T), \tag{2.10}$$

in order for the system to be thermodynamically stable for given (P,T).

This expression is linear with respect to the vector of concentrations $\{\bar{\psi}^j\}_{j=1}^{S}$ and so are the restrictions (2.8,2.9) thus one can apply linear programming to find the solution. One particular example for a two-component system is shown in the Figure 2.2.

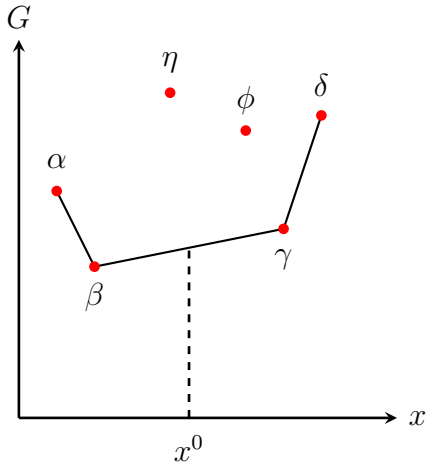

Figure 2.2: Example of 6 isochemical phases $\alpha, \beta, \gamma, \delta, \eta$, and ϕ in the $(G, \mathbf{X})$ space for a two-component mixture $\mathbf{X} = (x, 1-x)$. The black line represents the convex hull for given (P,T) conditions. For this particular choice of total composition $\mathbf{X}^0 = (x^0, 1-x^0)$, the system consists of a superposition of β and γ phases in accordance with the Gibbs phase rule.

Not all known phases have a fixed composition. This fact can be solved by the so-called solution models. The basic idea to parametrize the solution

as a superposition of a known set of p isochemical phases (end-points). The composition of a solution can be described by the barycentric coordinates in a p-simplex with the isochemical phases positioned in its vertices. The final Gibbs energy of the whole solution is then the weighted sum of the end-point values in the p-simplex corrected for the entropy of mixing term.

For computational purposes this parametrization is further discretized in a Cartesian manner into isochemical phases, which Connolly [2005] calls the pseudo-compounds. Then it is possible to increase the number of isochemical phases considered in the system. The linear minimization then explores a more densely occupied (G, X) space. An example of such parametrization in a two-component system is shown in the Figure 2.3. A detailed list of the solution phases considered in the Earth's mantle is discussed in the following section.

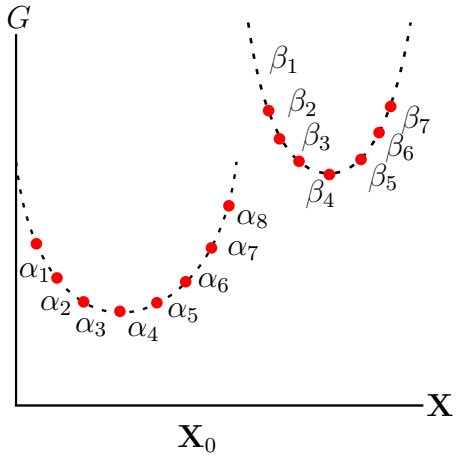

Figure 2.3: Solution models α and β represented in a two-component system. The solutions are respectively discretized into pseudo-compounds α_i and β_j. The values of G for $\alpha_2, \ldots, \alpha_7$ are interpolated from the end-point values α_1 and α_8 corresponding to the isochemical phases. Similar interpolation is applied also for β.

The Gibbs energy minimization is realized by the Perple_X software. Provided with a thermodynamic database describing the isochemical phases and database of the solution models, the Perple_X programs `verami` and `meemum` carry out the Gibbs energy minimization process for a given composition and (P, T) conditions. The resulting set of present phases and their concentrations is accompanied by selected physical properties, such as the seismic wave velocities and densities. However, the electrical conductivity of individual phases and the bulk electrical conductivity are not provided directly by Perple_X. Their calculation is the topic of Chapter 3 of this thesis. Further reading on the internal workings of `verami` and `meemum` programs can be found in Connolly [2009].

For future reference, I use this method as a deterministic part of the whole problem. I can retrieve the resulting molar phase fraction vector as a function of pressure temperature and composition $\psi^j(T, P, \mathbf{X})$.

2.2 Upper mantle modelling

In this work I will only model the suboceanic the upper mantle, ranging approximately from 35 km to 670 km under the Earths surface. Its composition excluding water can be approximated as a compound of the major oxides present. This so called CFMASN model consists of **C**aO, **F**eO, **M**gO, **A**l_2O_3, **S**iO_2, and **N**a_2O [Xu et al., 2008]. This sets the number of compounds to 6. The composition vector is defined by molar fraction, meaning that it has to be normalized. These constraints the vector only to 5 dimensions.

For construction of the approximate Gibbs energy function I will utilize the thermochemical database of Stixrude and Lithgow-Bertelloni [2005a,b], which operates in the CFMASN model. This database is available in Perple_X and is compatible with the default solution model file. For the purpose of modelling the upper mantle I consider only 5 permitted solid phases: olivine (ol), clinopyroxene (cpx), orthopyroxene (opx), C2/c pyroxene (C2/c) and garnet (gt). These minerals have to be described a set of solution models. Here I am using the solution models summarized in the Table 2.1.

Solution phase	Chemical composition	
ol[a]	$[Mg_xFe_{1-x}]_2SiO_4$	$0 \leq x \leq 1$
C2/c px[a]	$[Mg_xFe_{1-x}]_4Si_4O_{12}$	$0 \leq x \leq 1$
opx[a]	$[Ca_yFe_xMg_{1-x-y}]_2$	
	$\cdot[Fe_xAl_yMg_{1-x-y}]_2\ Si_4\ O_{12}$	$0 \leq x+y \leq 1$
cpx[a]	$[Ca_{1-x-y}Na_xMg_y]_2$	
	$\cdot[Fe_wMg_{y+z}Al_{1-x-y-w-z}]_2\ Si_4\ O_{12}$	$0 \leq x+y+z+w \leq 1$
gt[a]	$[\ (Na_{1/3}Al_{2/3})_w\ Fe_xCa_yMg_{1-w-x-y}]_3$	
	$\cdot[Mg_zAl_{1-z-w}Si_{w+z}]_2\ Si_2\ O_{12}$	$0 \leq x+y+z+w \leq 1$

Table 2.1: Chemical composition of solutions and isochemical phases as in a)Xu et al. [2008] and b)Stixrude and Lithgow-Bertelloni [2007]. Here w, x, y, z are the degrees of freedom.

2.3 Water content

The presence of water is not admitted within the framework of the CFMASN model. However, it plays an important role for the electrical conductivity of individual phases. After Khan [2016] I use the water content C_w as a separate parameter outside the Gibbs energy minimization process. It is defined as a point-wise weight percentage of water present in the phase mix. The water is not evenly distributed in all the resulting phases. A frequently used approximation of such distribution is to employ set of water partition coefficient defined as

$$D_{i/j} = \frac{C_w^i}{C_w^j}, \tag{2.11}$$

where C_w^i and C_w^j are the water contents of solid phase i and j respectively. Values of these coefficients can vary depending on the composition of the phase mix,

temperature and pressure. For the purpose of this study I omit these variations and consider them to be constant.

I am using a set of partition coefficients expressed in relation to the water content of olivine. In this case the bulk water content can be expressed as

$$C_w = \sum_i^s \psi_i C_w^i = C_w^{\mathrm{ol}}(\psi_{ol} + \psi_{cpx} D_{\mathrm{cpx/ol}} + \psi_{opx} D_{\mathrm{opx/ol}} + \psi_{C2/c} D_{\mathrm{(C2/c)/ol}} + \psi_{gt} D_{\mathrm{gt/ol}}), \tag{2.12}$$

where ψ_i is the molar fraction of the phase i. Used values for the partition coefficients are presented in the Table 2.2. Water partition coefficient of pyroxenes (orthopyroxene, clinopyroxene) are sourced from Demouchy et al. [2017]. Due to insufficient data describing the water partition of C2/c pyroxene in the upper mantle solid phase mix I set its partition coefficient relative to olivine to be the same as the partition coefficient of orthopyroxene. For garnet, I use the value of the partition coefficient derived in Novella et al. [2014].

i/j	$D_{i/j}$
cpx/ol	0.8
opx/ol	5.6
gt/ol	0.8

Table 2.2: Water partition coefficients for clinopyroxene, orthopyroxene and garnet with respect to olivine.

3. Mantle rock conductivity

This section contains the methods for obtaining the electric conductivity of the mantle rocks and their mix. Parts of this section are based on my Bachelor thesis Knopp [2021].

Most of the present mantle phases are silica-based and can be considered semiconductors. Their conductivity spans the range of 6 orders of magnitude, from 10^{-7}S/m to 10^{-1}S/m. There are three charge transport mechanisms contributing to the total conductivity of mantle phases: the ionic conductivity σ_i, the proton conductivity σ_p, and the small polaron hopping conductivity σ_h [Yoshino, 2010]. All of these mechanisms, if present, act in a parallel manner and the total conductivity of the phase is $\sigma \equiv \sigma(T, P, X_{\mathrm{Fe}}, C_w)$

$$\sigma = \sigma_i + \sigma_h + \sigma_p \,. \tag{3.1}$$

The ionic conductivity is the simplest conducting mechanism in mantle minerals. It is caused by the movement of ions between vacancies in the crystal lattice. A specific type of ionic conductivity is proton conductivity. It typically depends on the water content in the mineral. The water here provides the positive hydrogen ion as a charge transporting particle, where the proton hops between point defects in the crystal lattice.

In the case of small polaron hopping the charge carrier is a quasi particle called polaron, that moves (hops) between iron sites in the phase solution. Thus, the strength of the mechanism depends on the amount of iron in the mineral. The theory of small polaron hopping is further described in Triberis [2017].

Each conductivity term in the equation 3.1 depends also on temperature, and pressure. These dependencies can be parametrized by the activation energy (or enthalpy) and the activation volume in an Arrhenius-like expression. Their values as well as their dependencies on the water and iron content are determined experimentally from high pressure and temperature conductivity measurements.

3.1 Experimental values

In the environment of the upper mantle the most prevalent conductivity mechanism is the water dependent proton conductivity. Under the assumption that a measurable water content is present, $C_w > 0.001\%$, it is permissible to mostly neglect the ionic conductivity and focus only on water dependent terms.

The process of experimentally measuring the electric conductivity dependency on temperature, pressure and water content can be tricky. Due to the high pressure and temperature conditions, that create the major upper mantle oxides, the synthesis of the measured samples is very technically challenging. The synthesized samples need not be pure. In the case of more broadly defined mineral like olivine (as defined in Table 2.1) some free parameters of the solution can vary. This variation is in some cases measured and accounted for in the resulting electrical conductivity dependency, e.g. the amount of iron, that can influence the polaron hopping conductivity. Due to these challenges, the results of different experimental groups yield different sets of upper mantle mineral conductivity dependencies, varying not only as sets of parameters, but also as sets of fits.

When trying to model the electrical conductivity of the upper mantle, one has a large degree of freedom in the choice of lab derived results. I choose a set of the wet minerals electrical conductivity dependencies below based on the presence of error estimation for the measured fit parameters and on the viability of the models in the modelled pressure and temperature conditions used in this work.

The electric conductivity model for olivine presented in Xu et al. [2006] is purely water dependent model, described by only three parameters.

$$\sigma_{\mathrm{ol}} = C_w^r \sigma_{p0} e^{-\frac{H_p}{RT}}. \tag{3.2}$$

Similar model by Zhao and Yoshino [2016] is used for the clinopyroxene dependency.

$$C_w^r \sigma_{p0} e^{-\frac{H_p}{RT}}. \tag{3.3}$$

The model for orthopyroxene by Zhang et al. [2012] is the most parametrized, because the iron content independent polaron hopping mechanism is included for fitting the experimental data. Also, the activation enthalpy of the proton conductivity therm is non-constant and water dependent.

$$\sigma_{h0} e^{-\frac{H_h}{RT}} + C_w^r \sigma_{p0} e^{-\frac{H_p - \alpha C_w^{1/3}}{RT}}. \tag{3.4}$$

The only pressure dependent conductivity is that for garnet by Dai and Karato [2009]. This model includes activation volume for the proton conductivity term in the Arrhenius-like expression.

$$\sigma_{p0} C_w^r e^{-\frac{H_h + PV}{RT}}. \tag{3.5}$$

Values for all the parameters above are given in Table 3.1. The values include the error provided by the experimental studies, and it is taken at face value as a standard deviation of a normal distribution.

	$\log_{10}\left(\frac{\sigma_{p0}}{[\mathrm{S/m}]}\right)$	$\frac{H_p}{[\mathrm{kJ/mol}]}$	r	$\log_{10}\left(\frac{\sigma_{h0}}{[\mathrm{S/m}]}\right)$	$\frac{H_h}{[\mathrm{kJ/mol}]}$	$\frac{\alpha}{[\mathrm{kJ/mol}]}$	$\frac{V}{[\mathrm{cm^3/mol}]}$
ol	3.0(4)	87(5)	0.62(15)	-	-	-	-
cpx	3.69(15)	111(2)	1.28(5)	-	-	-	-
opx	2.58(14)	81(3)	-	3.99(23)	181(7)	0.08(3)	-
gt	3.29(16)	70(5)	0.63(19)	-	-	-	−0.57(5)

Table 3.1: Experimental values for the conductivity dependencies parameters.

3.2 Averaging mineral conductivities

Knowing the conductivities of present phases is just the first piece of the puzzle. The second one is to combine the phase conductivities into the total bulk conductivity of the phase mixture. When modelling the bulk conductivity of a phase mix the arrangement of the different components of varying conductivities is crucial. If, for example, the different mineral were formed into sheets and stacked on top of each other, the bulk conductivity would be also direction dependent and the simple scalar value used in the chapter 1 would not be applicable.

For now lets assume that bulk conductivity depends on the conductivities and volume fractions of the individual phases. For phases $j = 1, \ldots, s$ I denote the phase conductivities $\sigma_1, \ldots, \sigma_s$ and their volume fractions $c_1, \ldots, c_s$, which are related to the phase molar concentrations $\bar{\psi}^j$ through the scaling

$$c_j = \frac{M^j \bar{\psi}^j}{\rho^j} \Big/ \left(\sum_{i=1}^{s} \frac{M^i \bar{\psi}^i}{\rho^i} \right). \tag{3.6}$$

Here M^j is the molar weight and ρ^j is the density of the j-th phase.

The bulk conductivity can be obtained in infinitely many ways, depending on the spatial structure of the phase mixture and the direction of the electric current. By the nature of the sheet stacking example above one can try to constrain the bulk conductivity by this extreme case. The first is the minimal extreme of serially connected phases, where the bulk conductivity is the weighted harmonic average of the present phase conductivities.

$$\sigma_H = \left(\sum_{i}^{n} \frac{c_i}{\sigma_i} \right)^{-1} . \tag{3.7}$$

The second is the maximal extreme of bulk conductivity, where the phases are connected parallelly to each other in the direction of the current. Here the bulk conductivity is only the weighted arithmetic average of the present phase conductivities

$$\sigma_A = \sum_{i}^{n} c_i \sigma_i \, . \tag{3.8}$$

There exists a more complex approach to constrain the bulk electric conductivity, using so-called Hashin-Shtrikman (HS) bounds. For the construction of the HS bounds one has to assume the isotropic and maximally entropic configuration of the phases present. Such assumption is permissible for the unknown state of the upper mantle phase mix ruled by the laws of thermodynamics. Here I am using the following approximation for HS bounds used in Khan [2016],

$$\sigma^{\pm}_{HS} = \left(\sum_{i}^{n} \frac{c_i}{\sigma_i + 2\sigma_{\pm}} \right)^{-1} - 2\sigma_{\pm} \, . \tag{3.9}$$

Here $\sigma_{\mathrm{HS}\pm}$ denote the conductivity values for the lower HS_- and upper HS_+ bounds. The minimum and maximum conductivities present in the phase mixture are denoted by σ_- and σ_+, respectively.

Figure 3.1 illustrates the properties of the HS bounds for a simplified example of a two-phase mixture. Note that the weighted arithmetic average σ_{A} and weighted harmonic average σ_{H}, are also shown in the figure and lie outside the range of their respective HS bounds. As this Figure shows, the differences between the HS bounds are still large, but they are so far the best way to constrain the bulk conductivity.

By combining the bulk conductivity constrains with the lab derived parameters I present two bulk conductivity functions

$$\sigma_{\mathrm{HS}\pm}(T, P, C_w, \{\psi^j\}(T, P, \mathbf{X}), \{\alpha_i\}) = \sigma_{\mathrm{HS}\pm}(T, P, C_w, \mathbf{X}, \{\alpha_i\}_{i=1}^{m}). \tag{3.10}$$

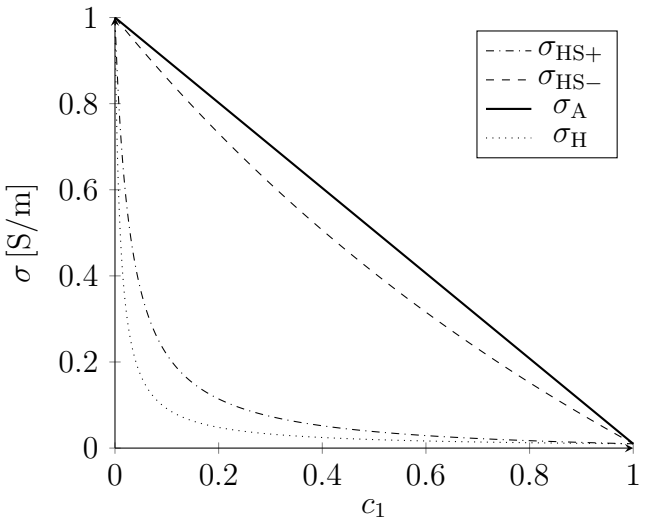

Figure 3.1: The HS bounds $\sigma_{\mathrm{HS}\pm}$, the weighted arithmetic average σ_{A} for a two phase mixture. The phases have the electrical conductivities $\sigma_1 = 0.01\,\mathrm{S/m}$ and $\sigma_2 = 1\,\mathrm{S/m}$ and volume fractions c_1 and $c_2 = 1 - c_1$, respectively.

These are the electric conductivity functions corresponding to the upper and lower HS bounds for given temperature T, pressure P, bulk water content C_w and chemical composition vector $\mathbf{X}$. The set $\{\alpha_i\}_{i=1}^{m}$ encodes the parameters, described in the Table 3.1, where m is the number of parameters.

4. Error propagation

In this chapter I present the basics of inverse problem theory as presented by Tarantola [2005] and methods for analyzing probability distributions resulting from the relevant inverse and forward problems.

Let's define a linear vector space $\mathcal{A}$ with an associated homogenous probability density $\mu_A(\mathbf{a}) : \mathcal{A} \to [0, \infty]$ such that for any probability density $\rho(\mathbf{a}) : \mathcal{A} \to [0, \infty]$, the probability of observing a variable in a measurable subset A is

$$M(A) = \int_A \rho(\mathbf{a}) \mu_a \, d\mathbf{a}. \tag{4.1}$$

For the purposes of inverse problems we define a model space $\mathcal{M}$ and a data space $\mathcal{D}$, with their respective homogenous probability densities $\mu_M(\mathbf{m}) : \mathcal{M} \to [0, \infty]$ and $\mu_D(\mathbf{d}) : \mathcal{D} \to [0, \infty]$. We can further use a Cartesian product of these spaces $\mathcal{M} \times \mathcal{D}$, which has a homogenous probability density $\mu(\mathbf{m}, \mathbf{d}) = \mu_M(\mathbf{m}) \times \mu_D(\mathbf{d})$.

For the purposes of modelling a physical phenomenon there has to be defined so-called joint probability density $\Theta(\mathbf{d}, \mathbf{m})$, describing the probability of observing both the data in state $\mathbf{d}$ and the model parameter in state $\mathbf{m}$. Furthermore, let's define a conditional probability density $\theta(\mathbf{d}|\mathbf{m}) : \mathcal{D} \to [0, \infty]$ as

$$\Theta(\mathbf{d}, \mathbf{m}) = \theta(\mathbf{d}|\mathbf{m}) \mu_M(\mathbf{m}) \,, \tag{4.2}$$

denoting the probability of observing the data in state $\mathbf{d}$ given a fixed model parameter $\mathbf{m}$.

The conditional density $\theta(\mathbf{d}|\mathbf{m})$ is encoding the forward modelling of the physical phenomenon. Let's define two prior probability densities $\rho_D(\mathbf{d})$ and $\rho_M(\mathbf{m})$, describing the knowledge of the data probability density and prior assumptions about the model parameters, respectively. Let's further define the joint prior probability density $\rho(\mathbf{d}, \mathbf{m}) = \rho_D(\mathbf{d}) \rho_M(\mathbf{m})$. Combining the prior probability density and the theoretical information in joint probability density yields their conjunction as a posterior probability density

$$\sigma(\mathbf{d}, \mathbf{m}) = K \frac{\rho(\mathbf{d}, \mathbf{m}) \Theta(\mathbf{d}, \mathbf{m})}{\mu(\mathbf{d}, \mathbf{m})} \,, \tag{4.3}$$

where K is a normalization constant. To get a solution to an inverse problem as a posterior probability density in the model space $\mathcal{M}$, the equation 4.3 needs to be integrated over the data space $\mathcal{D}$. This integration result in the following expression

$$\begin{aligned} \sigma_M(\mathbf{m}) &= K \int_D \frac{\rho(\mathbf{d}, \mathbf{m}) \Theta(\mathbf{d}, \mathbf{m})}{\mu(\mathbf{d}, \mathbf{m})} \mathrm{d}\mathbf{d} \\ &= K \int_D \frac{\rho_D(\mathbf{d}) \rho_M(\mathbf{m}) \theta(\mathbf{d}|\mathbf{m}) \mu_M(\mathbf{m})}{\mu_D(\mathbf{d}) \mu_M(\mathbf{m})} \mathrm{d}\mathbf{d} \\ &= K \rho_M(\mathbf{m}) \int_D \frac{\rho_D(\mathbf{d}) \theta(\mathbf{d}|\mathbf{m})}{\mu_D(\mathbf{d})} \mathrm{d}\mathbf{d}. \end{aligned} \tag{4.4}$$

It is useful to consider the case of exact data, where $\rho_D(\mathbf{d}) = \delta(\mathbf{d}_0 - \mathbf{d})$, where δ denotes the Dirac's delta distribution and $\mathbf{d}_0$ the exact data. In this case the model posterior probability density can be simplified to

$$\sigma_M(\mathbf{m}) = K \rho_M(\mathbf{m}) \theta(\mathbf{d}_0|\mathbf{m}). \tag{4.5}$$

4.1 Normal distribution approximation

For a well centered probability distribution $\rho(\mathbf{a}) : \mathbb{C}^n \to [0, \infty]$ of a variable $\mathbf{a}$ one can approximate it with a normal distribution

$$\rho(\mathbf{a}) \approx K \exp\left(-\frac{1}{2}(\mathbf{a}-\mathbf{a}_0)C^{-1}\overline{(\mathbf{a}-\mathbf{a}_0)}\right), \tag{4.6}$$

where the covariance matrix C is a hermitian matrix and $\mathbf{a}_0$ is the average value

$$\mathbf{a}_0 = \int \mathbf{a}\rho(\mathbf{a})\mathrm{d}\mathbf{a}. \tag{4.7}$$

The coefficients c_{ij} of the matrix C are defined as

$$c_{ij} = \int (\mathbf{a}-\mathbf{a}_0)_i \overline{(\mathbf{a}-\mathbf{a}_0)}_j \rho(\mathbf{a})\mathrm{d}\mathbf{a}. \tag{4.8}$$

For a finite number of data points, picked from the distribution ρ, the covariance matrix coefficients C_{ij} can be approximated as

$$c_{ij} = \frac{\sum (\mathbf{a}-\mathbf{a}_0)_i \overline{(\mathbf{a}-\mathbf{a}_0)}_j}{n}. \tag{4.9}$$

4.2 Propagation of laboratory measurements errors into electrical conductivity profiles

Let T_k and P_k be the temperature and pressure in k-th thermodynamically modelled layer, for $r \in [r_{k-1}, r_k]$. The temperature and pressure are assumed to have no lateral variations. Let C_w and $\mathbf{X}_0$ be the bulk water content and chemical composition vector, considered constant throughout the whole modelled mantle. For the purposes of this work, the only model variable in this setup is the water content. Due to non-negativity of the bulk water content C_w percentage, I represent the water content using a Jeffreys parameter $\mathbf{m} = \log_{10}(C_w)$, $\mathcal{M} = \mathbb{R}$. Although values of the water content percentage larger than 1 % do not make physical sense, due to water saturation, I will not restrict the model space from above.

The data space consists of the radial conductivity profiles. The electric conductivity is also a positive parameter, so the data space is also represented by vector Jeffreys parameter $\mathbf{d} = (\log_{10}(\sigma))_k$, $\mathcal{D} = \mathbb{R}^n$. For the model and data spaces defined like this, the homogenous probability density $\mu_M(\mathbf{m}) = 1$ and $\mu_D(\mathbf{d}) = 1$ are used.

To obtain conditional probability density $\theta(\mathbf{d}|\mathbf{m})$ for the forward problem from the end of Chapter 3 I have to contract this exact solution over the set of conductivity parameters from the Table 3.1. Let

$$\mathbf{d}(C_w, \{\alpha_i\}) = (\log_{10}(\sigma_k))_{k=0}^n = (\log_{10}(\sigma_{HS\pm}(T_k, P_k, \mathbf{X}_0)))_{k=0}^n(C_w, \{\alpha_i\}). \tag{4.10}$$

This denotes, that the vectors of the data space are dependent on the water content and the conductivity parameters. Meaning that each of the elements of a data vector shares the same set of the experimental conductivity parameters

$\{\alpha_i\}$. From now on I will be dropping the $HS\pm$ subscript meaning, there will be implicitly two versions of the forward problem.

Let each of the experimental conductivity parameters be taken out of a normal distribution

$$\rho_\alpha = Ke^{-\frac{(\alpha_i-\mu_{\alpha_i})^2}{2\sigma^2_{\alpha_i}}}, \tag{4.11}$$

where μ_{α_i} and σ_{α_i}, the mean and the standard deviation, are taken directly from the Table 3.1. Now the conditional probability distribution is

$$\theta(\mathbf{d}|\mathbf{m}) = K\int_{\mathbb{R}^m}\delta(\mathbf{d}-\mathbf{d}(C_w,\{\alpha_i\}))e^{-\sum_i\frac{(\alpha_i-\mu_{\alpha_i})^2}{2\sigma^2_{\alpha_i}}}\mathrm{d}\alpha, \tag{4.12}$$

where again K denotes some normalization constant.

To get a numerical approximation of this distribution I use a Monte Carlo approach by sampling the parameters α from their respective normal distribution using the Box-Muller algorithm. Using such method one can obtain on demand a single sample from the distribution 4.12.

To approximate the inverse problem solution i.e. to obtain the posterior distribution for $\mathbf{m} = \log_{10}(C_w)$, given exact data-point $\mathbf{d}_0 = (\log_{10}(\sigma_0))_k$, I use the Metropolis-Hastings algorithm. Firstly, I need to define the prior distribution for the water content. I assume only a realistic range of the water content to be $0.001\% < C_w < 0.1\%$ and the distribution in this range to be homogenous for $\log_{10}(C_w)$. This means that

$$\rho_M(\mathbf{m} = \log_{10}(C_w)) = \begin{cases} \frac{1}{-1-(-3)}, & -3 < \log_{10}(C_w) < -1 \\ 0 & \text{otherwise} \end{cases}. \tag{4.13}$$

Furthermore, I am only able to sample the conductivity from the conditional probability and not the other way around, in the case of a real computation. For this I will approximate the 4.12 by a normal distribution for a given $\mathbf{m}$. I can, for the given parameter $\mathbf{m}$, compute the average $\mu_{D,\mathbf{m}}$ and the covariance matrix $C_{D,\mathbf{m}}$. This can be achieved using a large, but finite, number of samples from the conditional distribution $\theta(\mathbf{d}|\mathbf{m})$. Now I can directly compute the approximate conditional probability as

$$\hat{\theta}(\mathbf{d}|\mathbf{m}) = Ke^{\frac{1}{2}(\mathbf{d}-\mu_{D,\mathbf{m}})C^{-1}_{\mathbf{d},\mathbf{m}}(\mathbf{d}-\mu_{D,\mathbf{m}})}, \tag{4.14}$$

where again K denotes some normalization constant.

Now I can finally get to run the Metropolis-Hastings algorithm to sample the discrete posterior probability distribution

$$\hat{\sigma_M}(\mathbf{m}) = K\rho_M(\mathbf{m})\hat{\theta}(\mathbf{d} = \mathbf{d}_0|\mathbf{m})\,. \tag{4.15}$$

I start by picking a random $\mathbf{m}^0$ from the uniform prior distribution ρ_M. I repeat the sampling to get a new $\mathbf{m}'$. Next, I compute the fraction of their conditional probability

$$p_0 = \frac{\hat{\theta}(\mathbf{d} = \mathbf{d}_0|\mathbf{m}')}{\hat{\theta}(\mathbf{d} = \mathbf{d}_0|\mathbf{m}^0)}. \tag{4.16}$$

If $p_0 \geq 1$, I accept the next sample $\mathbf{m}'$ and set $\mathbf{m}^1 = m'$ and if $p_0 < 1$, I accept m' with the probability of p_0, otherwise I reject it and set $m^1 = m^0$. This process repeats for many $\mathbf{m}^n$. This final set of model parameters $\{\mathbf{m}^n\}$ will approximate the posterior distribution for the water content $\hat{\sigma_M}(m_i)$.

4.3 Propagation of laboratory measurements errors into tidally induced magnetic field

In this case the data space represents the magnetic field of M2 tides. It is impossible to measure the magnetic field everywhere. Realistically, the only observable part of the field is on the surface and above it. The data space then describes the vector of internal coefficients $\mathbf{d} = (G_{jm}^{(i)})$, coupled to the surface magnetic field $\mathbf{B}$ using the formula

$$G_{jm}^{(i)} = \frac{B_{jm}^{(-1)}(a) - jB_{jm}^{(1)}(a)}{2j+1}\,. \tag{4.17}$$

In an experimental setting the internal field coefficients are obtained for example by analysis of Swarm and CHAMP satellite magnetic measurements [Šachl et al., 2024, 2022]. In particular, I refer to the GO19 model obtained by dedicated inversion method by Grayver and Olsen [2019], and the MTI family of models stemming from a comprehensive approach [Sabaka et al., 2020].

I can set the data space to be $\mathcal{D} = \mathbb{C}^{j_{\max}(j_{\max}+2)}$. The associated data space homogenous distribution is considered to be trivial, as in the previous cases.

I denote the solution for the EMI forward modelling as

$$\mathbf{d} = (G_{jm}^{(i)}) = \mathbf{G}^{(i)}((\sigma_k)), \tag{4.18}$$

where the input variables like the internal forcing $\mathbf{E}_{imp}$ are considered to be constant. The only variable is the electric conductivity. In this case the conductivity entering into the EMI model is assumed to be only radial, with no lateral variations.

The model space still describes the water content $\mathbf{m} = \log_{10}(C_w)$ and has the same properties as in the previous case. The thermodynamic and conductivity model are only valid for a section of the upper mantle. Due to this limitation of the forward problem for the electrical conductivity, the calculated model has to be combined with some background model σ_0^k. The conductivity coefficients used in the EMI forward problem can be then set as

$$\sigma_k(C_w, \{\alpha_i\}) = \begin{cases} \sigma_k(C_w, \{\alpha_i\}), & k_s < k < k_e \\ \sigma_0^k, & \text{otherwise} \end{cases}, \tag{4.19}$$

where $k_s < k_e$ indexes of the lowermost and uppermost thermodynamically modelled layers.

The conditional distribution for this problem is set to be

$$\theta(\mathbf{d}|\mathbf{m}) = K \int_{\mathbb{R}^m} \delta(\mathbf{d} - \mathbf{G}^{(i)}((\sigma_k(C_w, \{\alpha_i\})))) e^{-\sum_i \frac{(\alpha_i - \mu_{\alpha_i})^2}{2\sigma_{\alpha_i}^2}} \mathrm{d}\alpha\,. \tag{4.20}$$

It is important to mention, that also in this case, there are two forward problems, each corresponding to one of the HS bounds.

I will not be exploring the associated inverse problem, due to computational limitations, but in the next section I will present the conditional distribution in terms of normal distribution approximation.

5. Results

In this section I will present the results of the forward and inverse modelling for the synthetic conductivity model and the forward modelling of the EMI model for the synthesized conductivity as described in the previous section. It is necessarily to further specify the parameters of the thermodynamic model, temperature T_k, pressure P_k and chemical composition $\mathbf{X}$ and the modelled layers themselves.

Firstly the thermodynamically modelled layers each span the depth 20 km and their centers range from the depth of 93 km to 393 km, bellow the ocean surface. The pressure profile is sourced from the PREM model [Dziewonski and Anderson, 1981]. The pressure depth dependence is shown in the Figure 5.1a. The temperature and chemical composition is obtained from the thermochemical WINTERC-G model [Fullea et al., 2021]. The WINTERC-G model maps the whole upper mantle in terms of temperature and chemical composition, constructed using gravity, seismic and thermal data. Due to the 3D nature of this model I only use the lateral average values for every depth layer. The 1D temperature profile is shown in the Figure 5.1b. The chemical composition is almost constant in the radial direction. The constant value of the chemical composition is presented in the Table 5.1.

The thermochemical model computes the volume fraction of the major upper mantle phases for each modeled layer. The calculated phase profile is shown in the Figure 5.2 in terms of depth and volume fractions.

	X_w
CaO	3.93
FeO	8.05
MgO	37.8
Al_2O_3	4.52
SiO_2	45.7
Na_2O	0.0

Table 5.1: Values of chemical composition used in the thermodynamic model expressed in weight percentages.

5.1 Synthetic mantle conductivity profiles

Now I can combine the thermodynamic model with the conductivity model. To sample the conditional probability distributions, from the equation 4.12, for a given water content, I am using a Monte Carlo method to average over 100000 samples. The resulting distributions are represented as histograms with the average conductivity shown. Such histograms are computed for both the upper and lower HS bound of the bulk electric conductivity. I have chosen a set of four water content values to showcase the impact of the water content on the bulk electric conductivity. The values of water content are 10 ppm, 60 ppm, 210 ppm and 300 ppm. The histograms of the upper and lower HS bounds for the selected water content values are shown in the Figures 5.4, 5.5, 5.6 and 5.7. The Figure 5.3

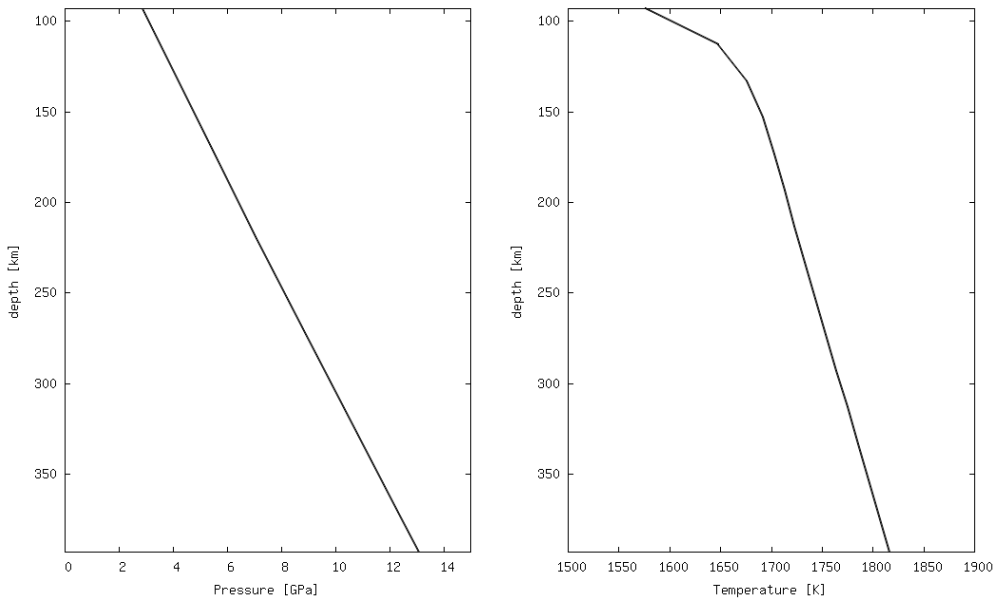

(a) Pressure profile from the PREM model for the given depth range.

(b) Average temperature profile from the WINTERC-G model.

Figure 5.1: Used temperature and pressure values for the conductivity and thermodynamic model.

shows all the average values for the lower and upper HS bounds for the selected water content values.

By comparing the histograms I can deduce several observations about the probability distribution. A first trivial observation is that for larger water content the conductivity rises. This is obvious from the equations 3.2 to 3.5. The second observation visible just from these histograms is, that the lower HS bound is always better defined that the upper HS bound for a given water content.

These histograms for each layer do not encode the correlations between the bulk conductivities in different depths. For this purpose I have also constructed the covariance matrices of the conditional probability distributions for each of the selected water contents, presented in the Figures 5.8 and 5.9 for the lower and upper HS bounds. The layers on these graphs are numbered from 0, corresponding to the lowermost depth 393 km, to 15, corresponding to the uppermost depth 93 km. The largest variance can be observed for the lowermost layers. The off-diagonal elements of the covariance matrices are always positive and comparable to the diagonal elements. This implies that large jumps between the layers are improbable. In a full EMI to conductivity inversion schema, like the one in Šachl et al. [2024], similar property of the resulting conductivity profile is enforced by a gradient regularization as a prior model distribution.

5.2 Posterior water inversion

With the ability to construct the covariance matrix of the conditional probability I can try to solve the inverse problem in terms of water posterior probability distribution in terms of the equation (4.15). I will do an experiment on a set of synthetic conductivity profiles.

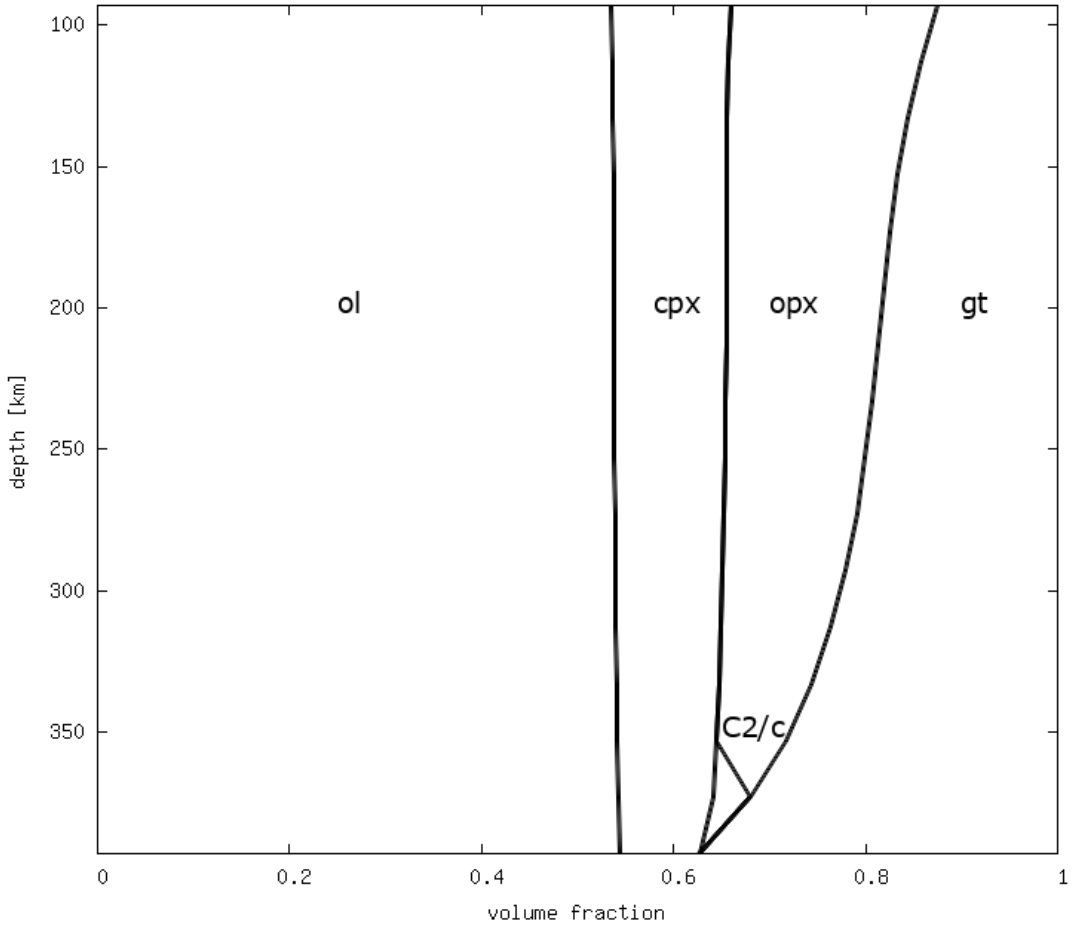

Figure 5.2: Phase profile showing volume fractions of the present phases

Firstly I will invert two profiles, the average lower and upper HS bounds for reasonable water content value $C_w = 210\,\text{ppm}$. These profiles are my exact data points. I will calculate the posterior distribution of the water content for the upper HS forward problem, where the exact data is the average of the upper HS bound for $C_w = 210\,\text{ppm}$. The same is done for the lower HS problem, with respect to the average lower HS bound. Graphs of these trivial inversions are shown in figure 5.10a.

This first synthesis problem shows again that the upper HS forward problem has lower resolution (the distribution is more spread out) than the lower HS problem. The other observation is that this inverse problem result in a wide spans of probable water content values, where the approximate standard deviation of the posterior distributions is on the scale of 0.1 $\log_{10}(wt\%)$.

Now I will compare the lower and upper HS forward problems on the same data set. I will take the $\log_{10}$ average of the average lower and upper HS bounds as the exact data for the conductivity profile. This resulting posterior probabilities for this synthetic inversion are shown in Figure 5.10b. This last Figure shows the inverse relation between the HS bounds and water content. The posterior water content distribution for upper HS bound represent the distribution of the lower water content estimate. Inversely the posterior water content distribution for the lower HS bound represent the distribution of the upper water content estimate.

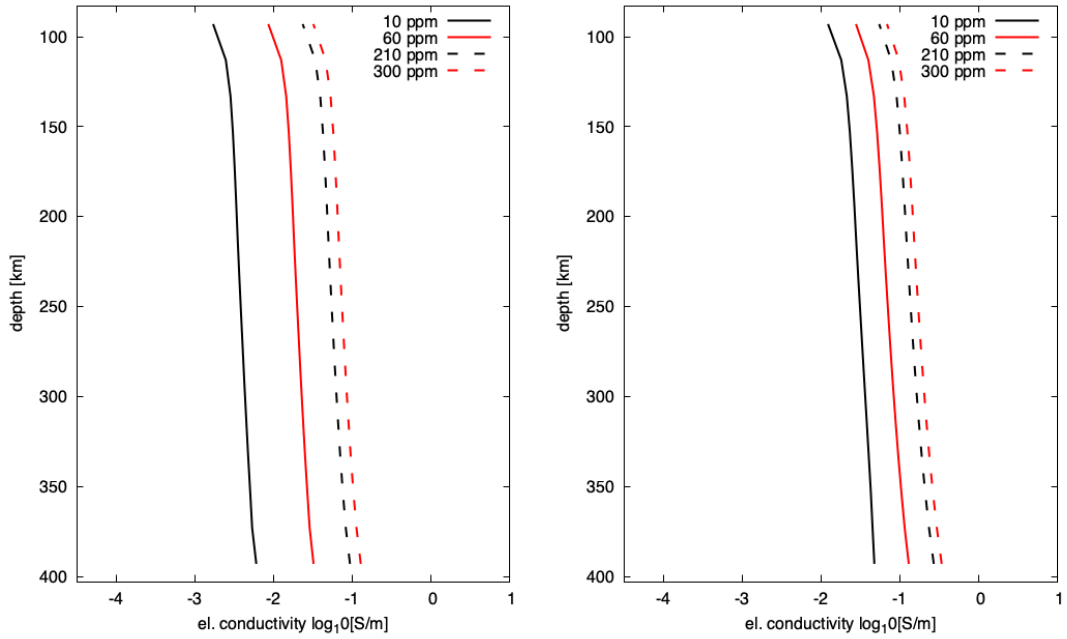

Figure 5.3: Profiles of the average HS lower(left) and upper(right) bounds for all the selected water content values.

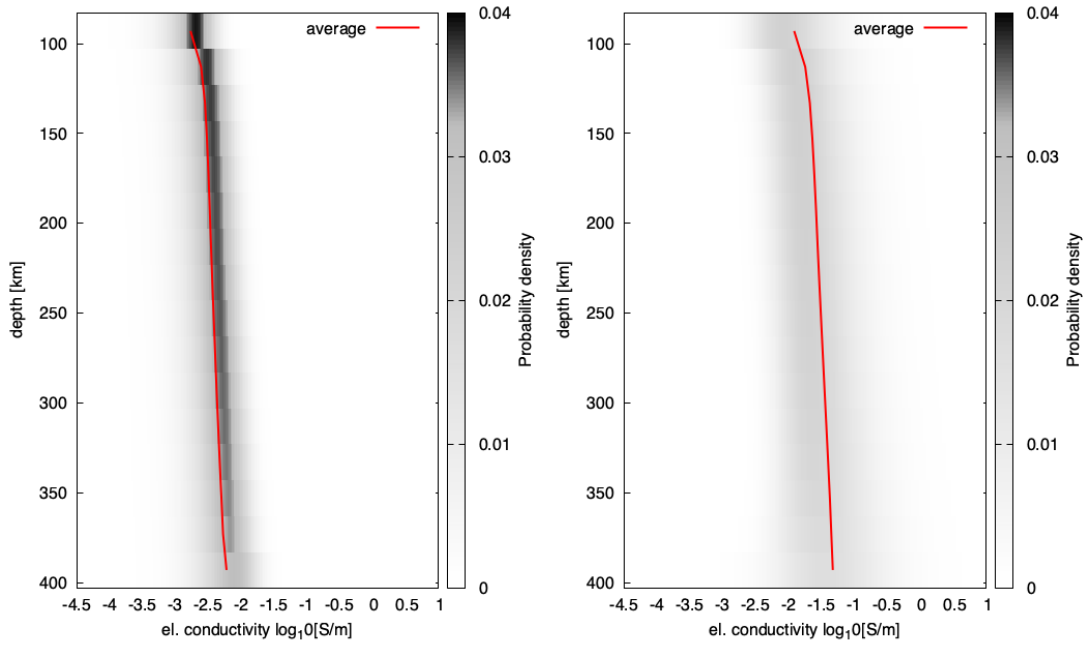

Figure 5.4: Probability distributions of lower(left) and upper(right) HS bounds for 10 ppm

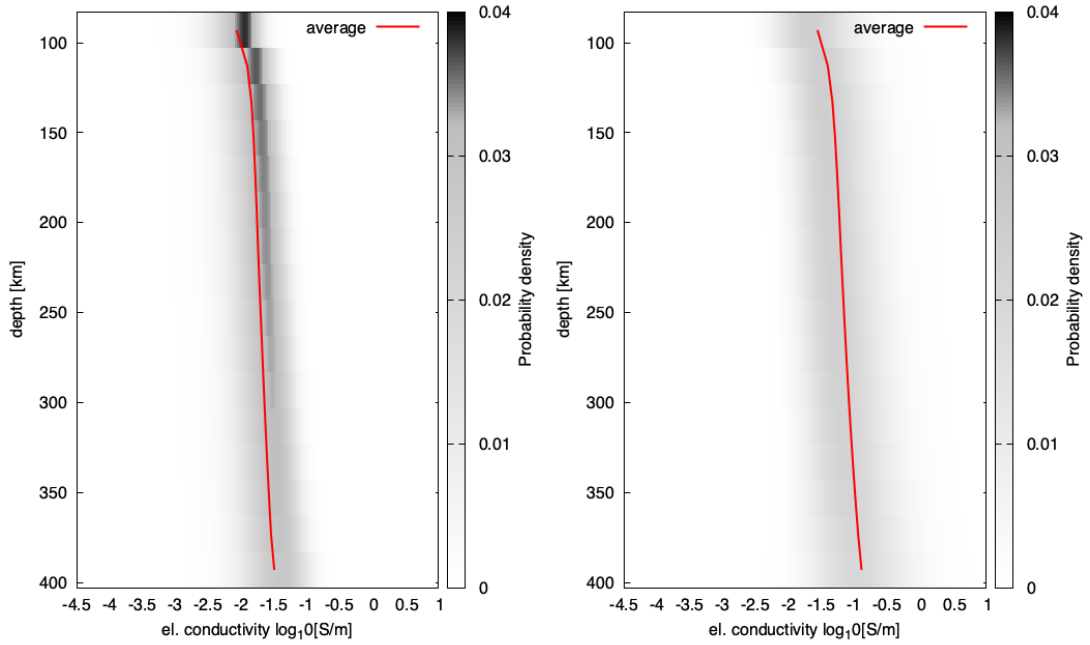

Figure 5.5: Probability distributions of lower(left) and upper(right) HS bounds for 60 ppm

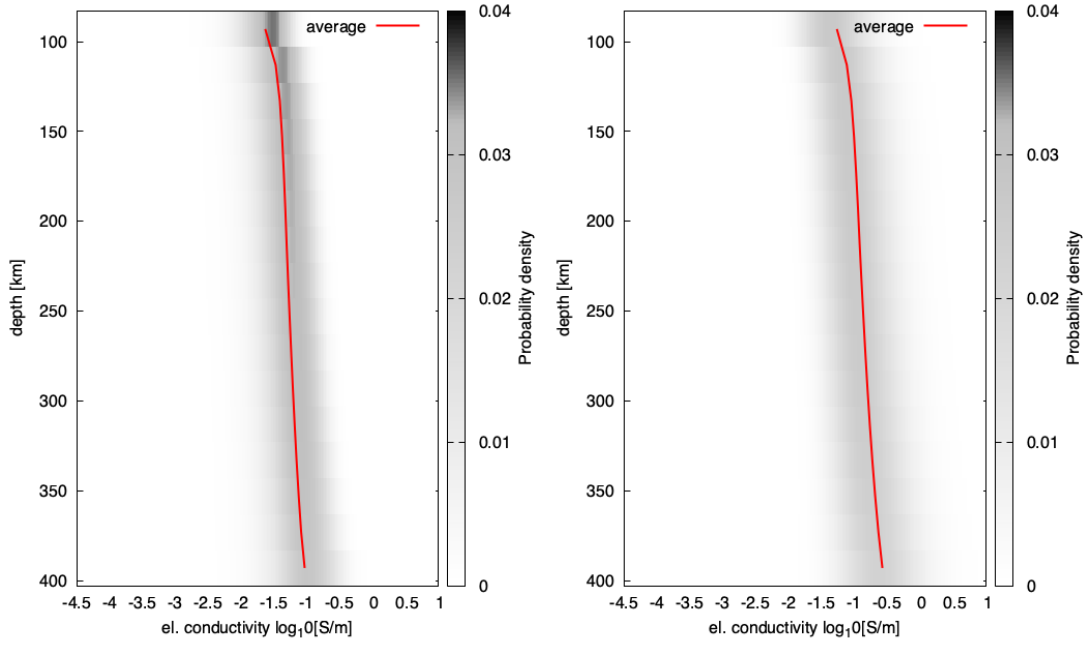

Figure 5.6: Probability distributions of lower(left) and upper(right) HS bounds for 210 ppm

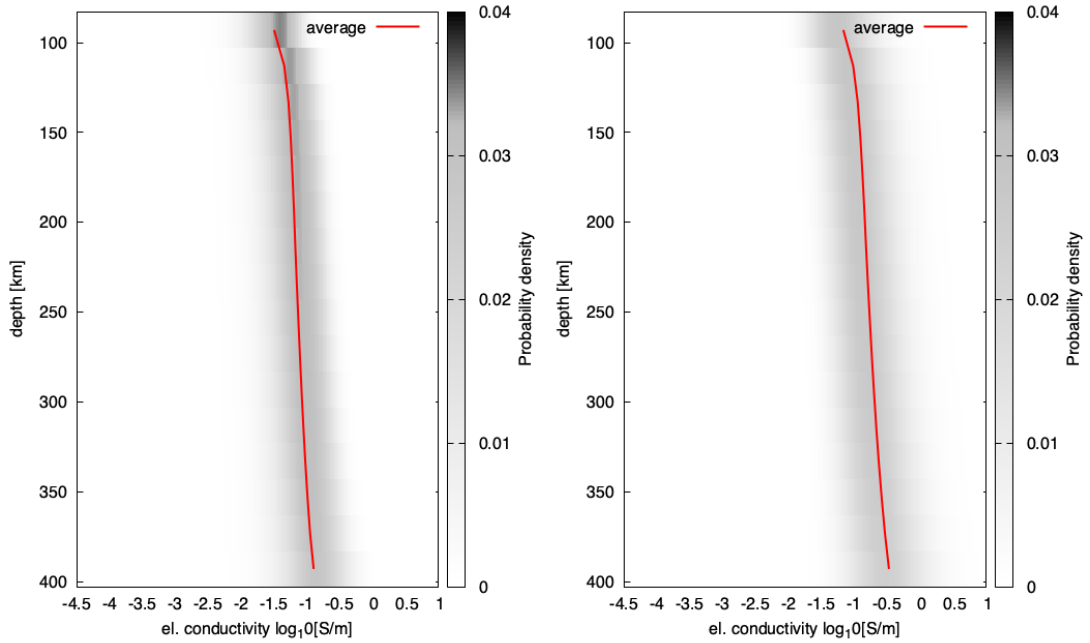

Figure 5.7: Probability distributions of lower(left) and upper(right) HS bounds for 300 ppm

5.3 Error propagation through the EMI model

To compute the conditional probability for the internal field coefficient ($G_{jm}^{(i)}$) I will first have to set up the EMI model. Firstly, I will set the background model $\sigma_0(r)$ as mentioned in the equation 4.19. I will use a 1D conductivity background model, constructed by averaging the suboceanic parts of the 3-D conductivity model WINTERC-e Wd-emax [Martinec et al., 2021]. This 1D reduction of the background model is shown in the Figure 5.11. The model spans the whole radius of the Earth.

The whole EMI model is computed on 204 layers, which are mostly concentrated in the crust and upper mantle. The SH cut-off $j_{max} = 20$. The thermodynamically modeled layers are the ones from the previous section.

I have computed the solution of the EMI forward problem for each of the previously shown conductivity profile distributions, synthesized for the water content values $10, 60, 210, 300$ ppm. After sampling the resulting internal field coefficient $G_{jm}^{(i)}$ for each of the water content values I interpreted them only in the terms of the average and covariance matrix. The average values can be comprehensively interpreted using Lowes-Mauersberger(LM) spectra as defined in Sabaka et al. [2016]. This spectrum reduces the directional indexes m and expresses the magnetic power of the SH order j as

$$R_j = 4\pi \frac{j+1}{2j+1} \left(\frac{1}{2} |G_{j0}^{(i)}|^2 + \sum_{m=1}^{j} |G_{jm}^{(i)}|^2 + |G_{j-m}^{(i)}|^2 \right). \tag{5.1}$$

The Lowes-Mauersberger spectra of the average $G_{jm}^{(i)}$ coefficients for models with different water content values are shown in the Figure 5.12 for lower HS bound and in the Figure 5.13 for upper HS bound. These spectra can be compared to

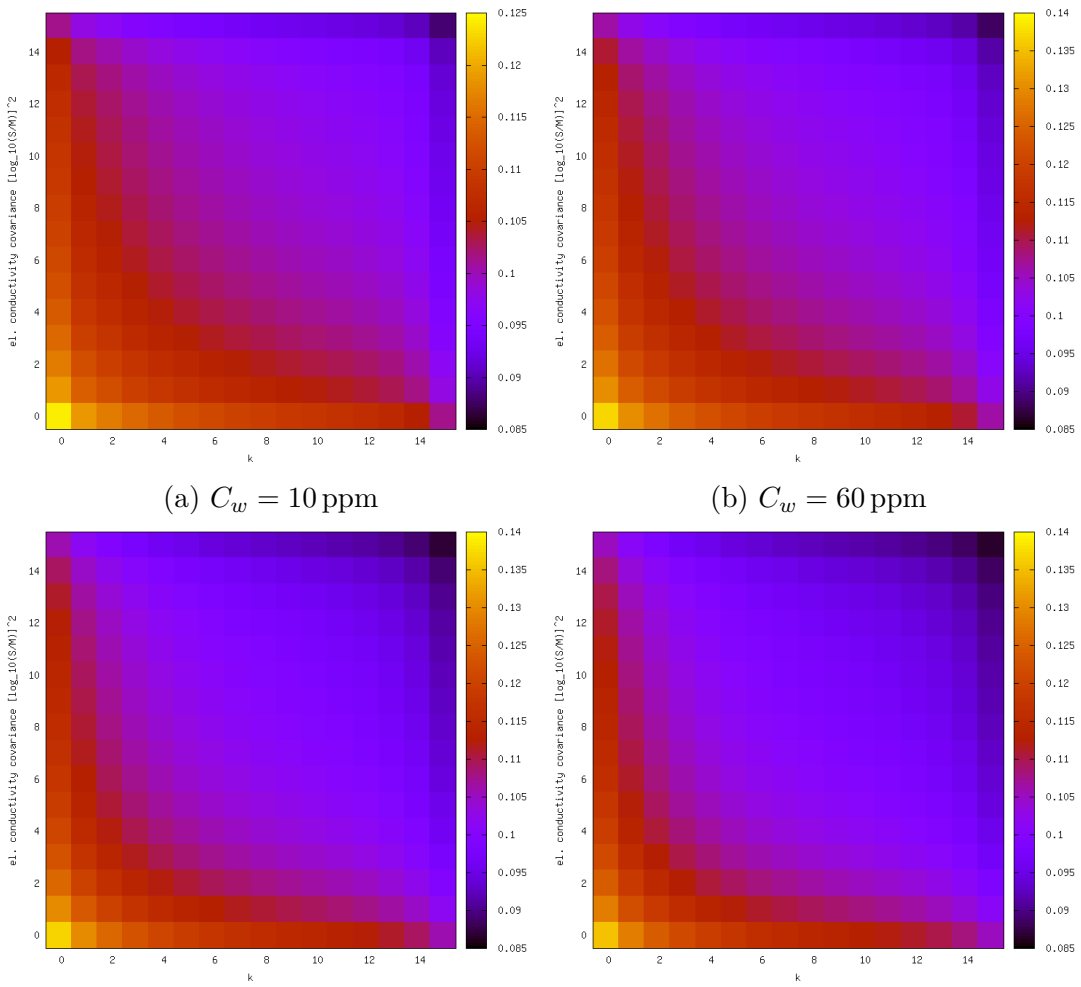

(a) $C_w = 10\,\text{ppm}$ (b) $C_w = 60\,\text{ppm}$

(c) $C_w = 210\,\text{ppm}$ (d) $C_w = 300\,\text{ppm}$

Figure 5.8: Covariance matrix for the probability distributions of lower HS bound forward problem for differences water content values. The matrix indexes correspond to the layer coefficients k, where $k = 0$ corresponds to the lowermost layer and $k = 15$ to the uppermost layer.

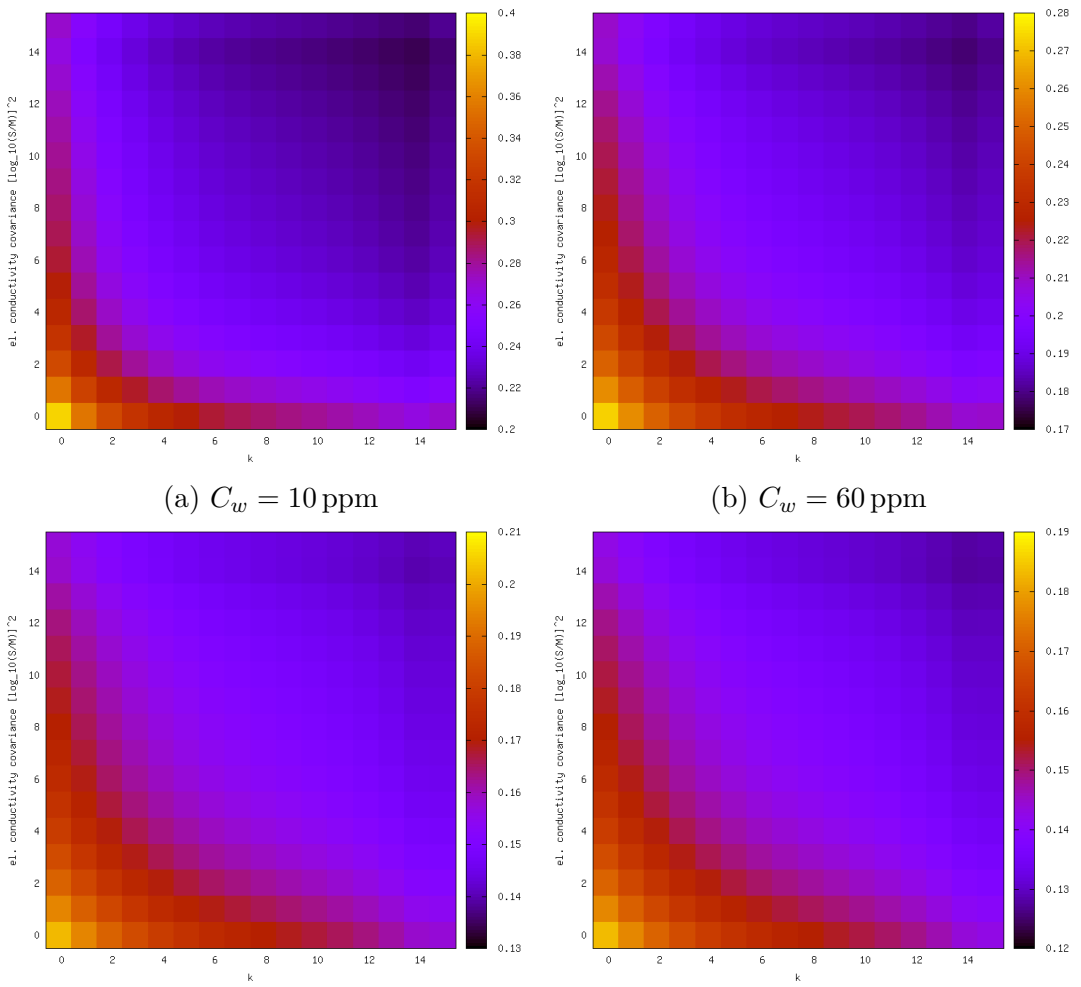

(a) $C_w = 10\,\text{ppm}$ (b) $C_w = 60\,\text{ppm}$

(c) $C_w = 210\,\text{ppm}$ (d) $C_w = 300\,\text{ppm}$

Figure 5.9: Covariance matrix for the probability distributions of upper HS bound forward problem for differences water content values. The matrix indexes correspond to the layer coefficients k, where $k = 0$ corresponds to the lowermost layer and $k = 15$ to the uppermost layer.

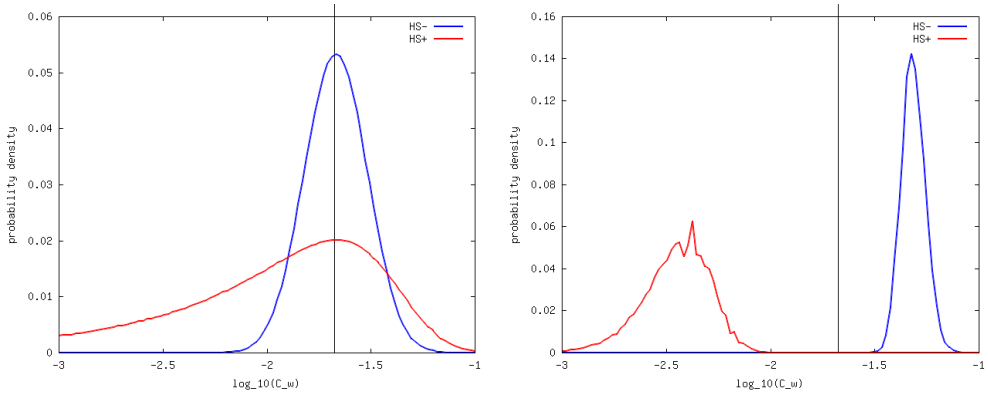

(a) Inversion of the upper and lower forward problems with respect to the synthetic lower and upper HS average profiles.

(b) Inversion of the upper and lower forward problems with respect to the $\log_{10}$ average of the lower and upper HS average profiles.

Figure 5.10: Posterior water content distributions as an inversion of synthetic conductivity profiles. The water content $C_w = 210\,\text{ppm}$ is denoted on the graphs as a vertical black line.

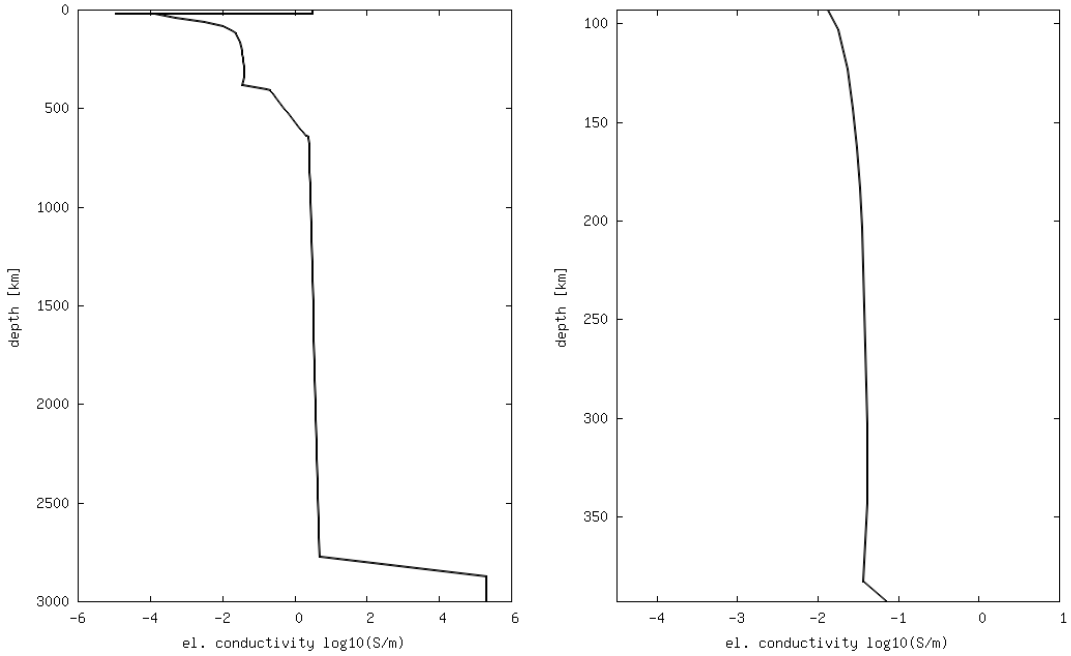

Figure 5.11: The background model We-max replaced by the synthetic conductivity distributions for the modelled depth range. The full conductivity profile is on the left and a zoom in on this profile is shown on the right.

the ones presented in Šachl et al. [2022]. The Figure 5.14, which has been taken over from Šachl et al. [2022], shows the LM spectra of M2 tidal magnetic internal field coefficients for measurements taken by the Swarm and CHAMP satellites as processed in the G019 dataset [Grayver and Olsen, 2019] and in the MTI family of datasets [Sabaka et al., 2020], labeled MTI601–MTI901, using 6 to 9 years of Swarm data. The Figure also shows the EMI response for the WINTERC-e Wd-emax 3D model [Šachl et al., 2022]. It is obvious, that the 1D EMI model used

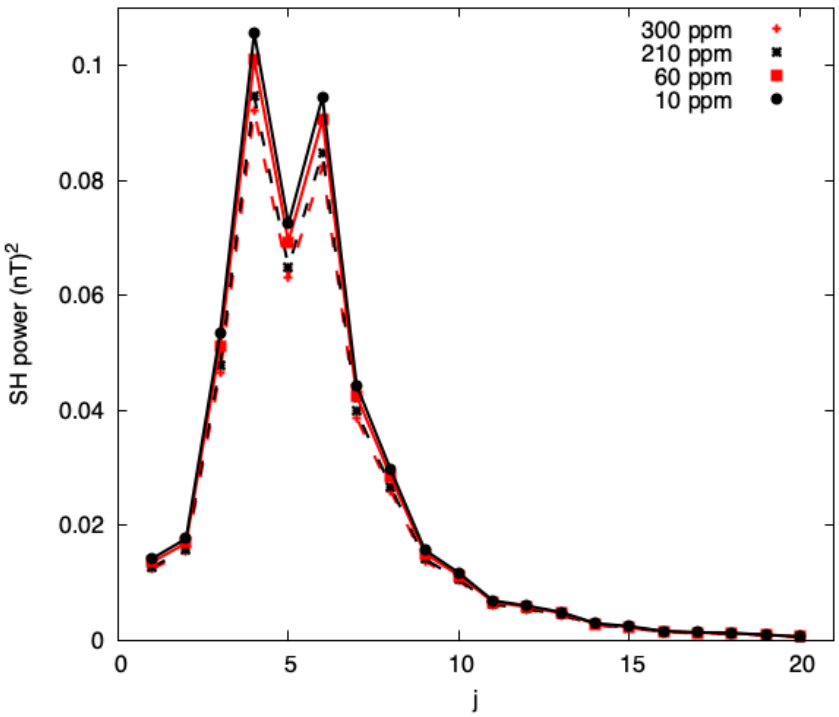

Figure 5.12: LM spectra of average internal magnetic field coefficients for the lower HS bound conductivity models.

here does not yield the same results as the 3D WINTERC-e Wd-emax model, this can be seen for the SH orders $j = 4, 6$. The orders of magnitude of these internal field coefficients are similar to the ones from the 1D EMI computation for the conductivity models synthesis by me.

The last result for of the EMI forward modelling are the covariance matrices for the calculated $G_{jm}^{(i)}$ coefficients. These matrices are presented in the figures 5.15 and 5.16 for the lower and upper HS bound forward problem, respectively.

The patterns of correlation and anti-correlation are independent on the water content and the type of forward model. The main takeaway from these covariance matrices is that the maximal variance can range from $0.01\,\mu\mathrm{T}^2$ to $10\,\mu\mathrm{T}^2$.

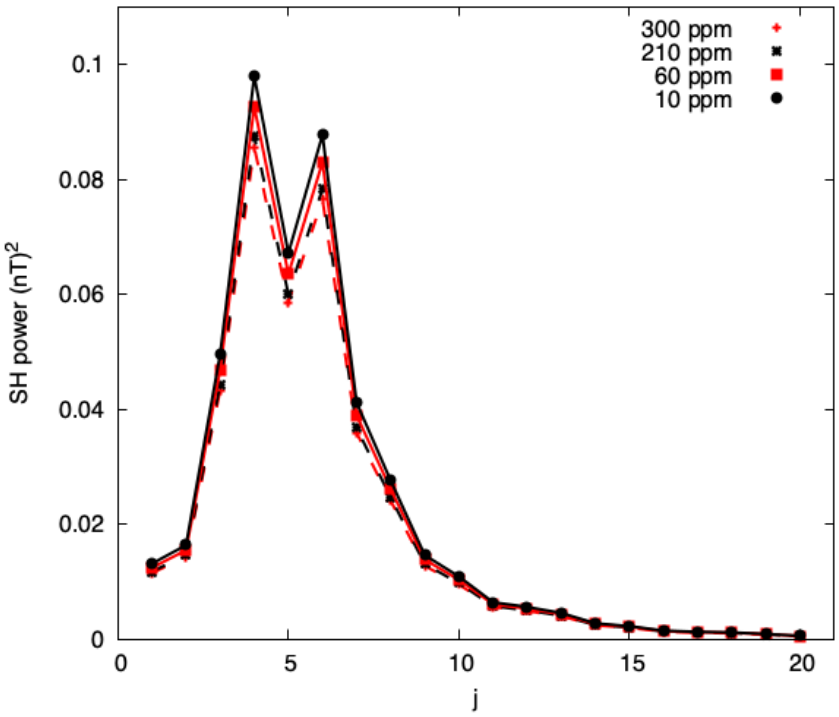

Figure 5.13: LM spectra of average internal magnetic field coefficients for the upper HS bound conductivity models.

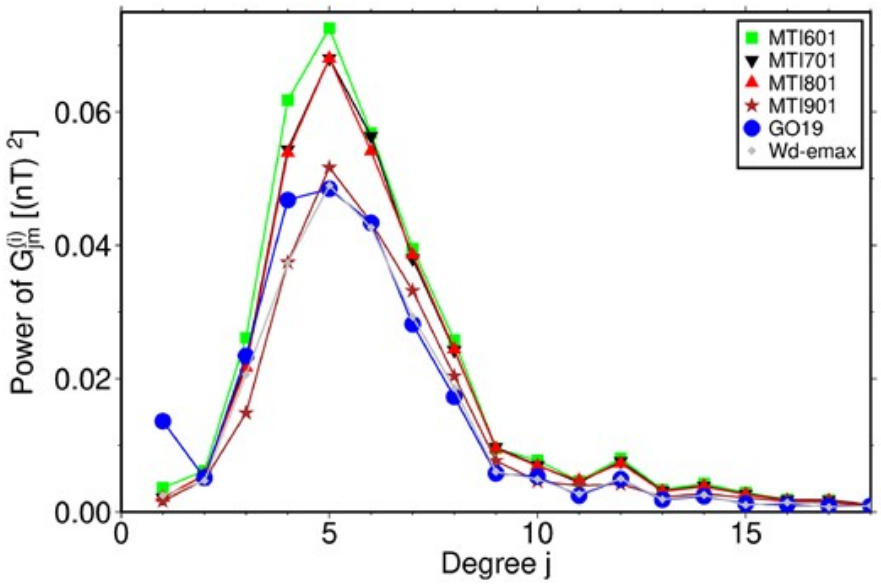

Figure 5.14: LM spectra for different experimental and synthesized dataset of the internal M2 magnetic field coefficients constructed by Šachl et al. [2022]

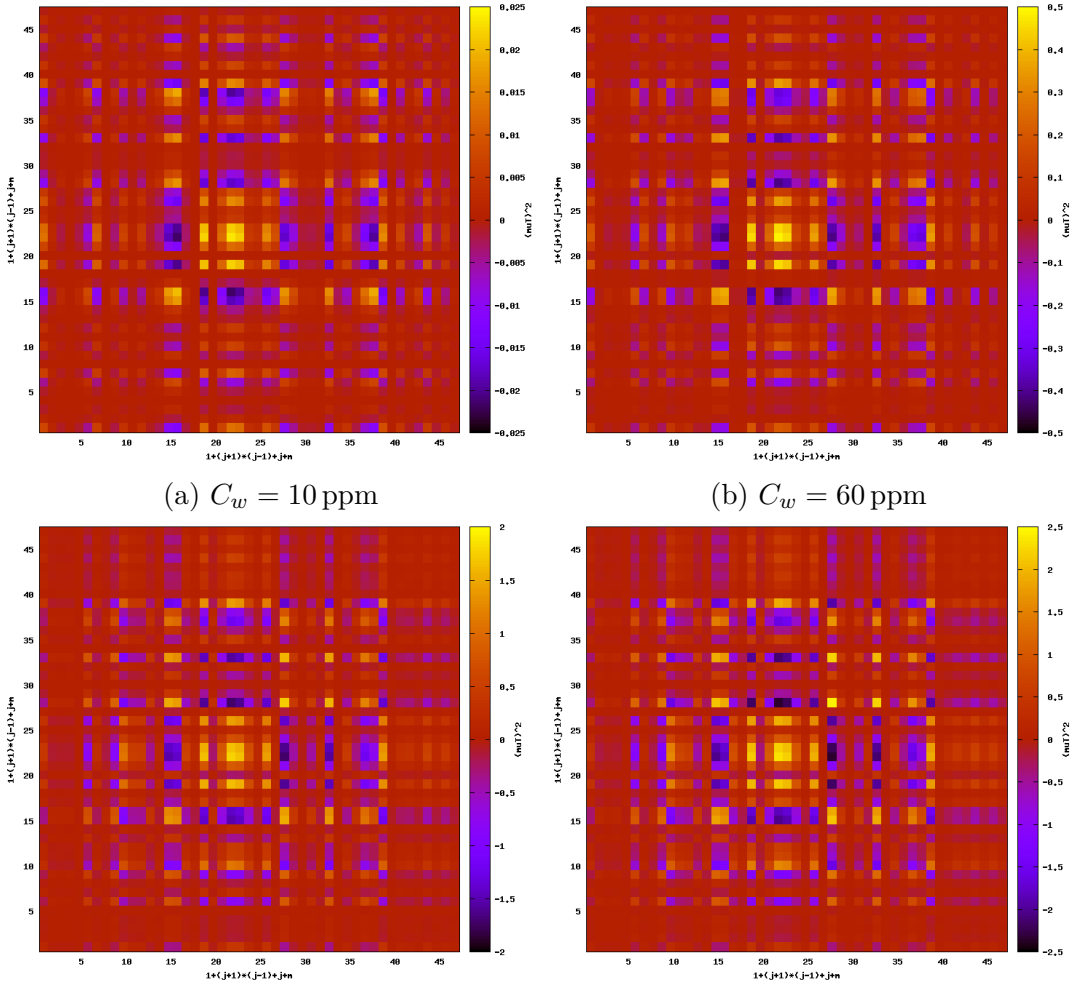

(a) $C_w = 10\,\text{ppm}$ (b) $C_w = 60\,\text{ppm}$

(c) $C_w = 210\,\text{ppm}$ (d) $C_w = 300\,\text{ppm}$

Figure 5.15: Real part of the covariance matrix for the probability distributions of $G_{jm}^{(i)}$ coefficients for the lower HS bound forward problem. The matrix uses a joint SH index $n = (j-1)(j+1) + j + m + 1$.

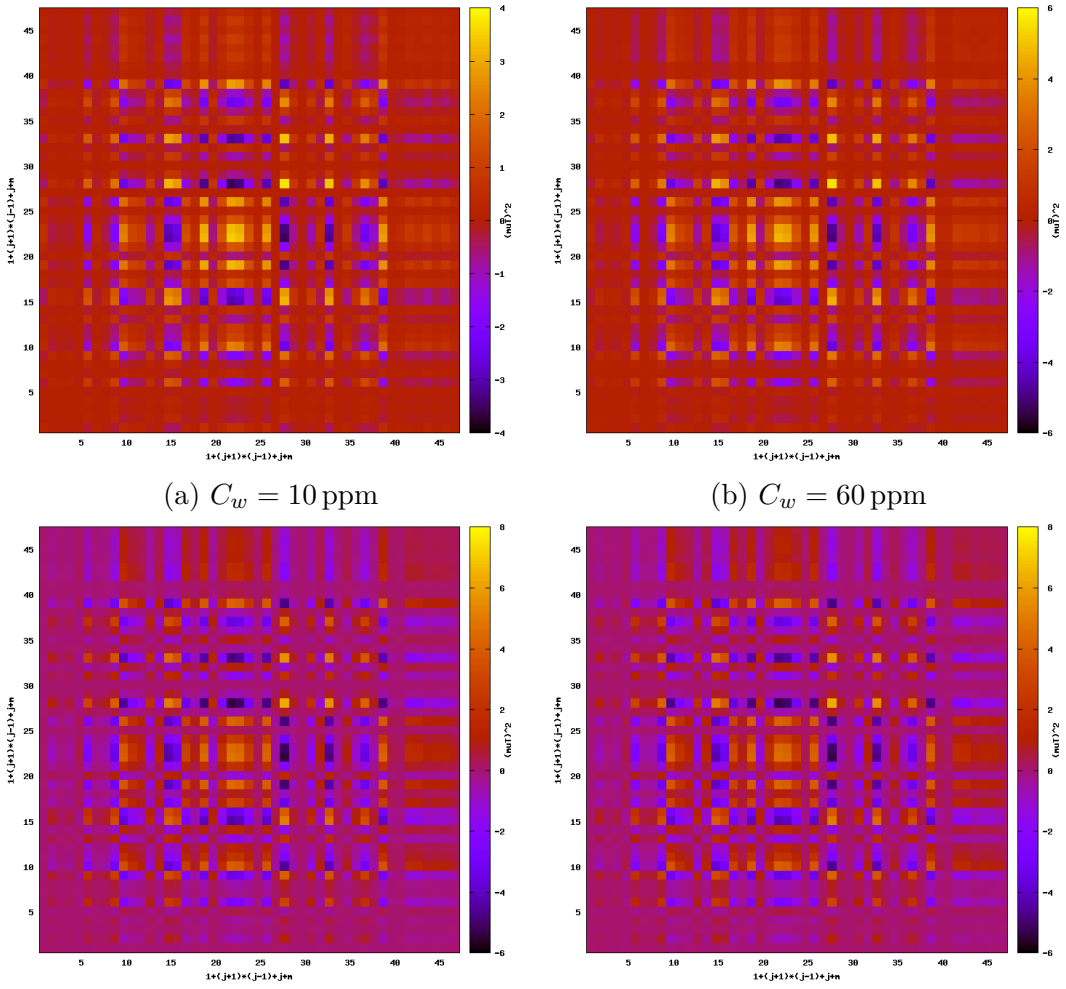

(a) $C_w = 10\,\text{ppm}$ (b) $C_w = 60\,\text{ppm}$

(c) $C_w = 210\,\text{ppm}$ (d) $C_w = 300\,\text{ppm}$

Figure 5.16: Real part of the covariance for the probability distributions of $G_{jm}^{(i)}$ coefficients for the upper HS bound forward problem. The matrix uses a joint SH index $n = (j-1)(j+1) + j + m + 1$.

Conclusion

I have demonstrated a Bayesian approach to the approximation of the error propagation of the lab-based mantle rock conductivity measurements through the synthetic conductivity of the upper mantle and its magnetic response to the M2 tidal forcing.

The error of the current lab based measurements of the upper mantle rocks is amplified by the bulk conductivity computation. The resulting variances of these bounds for log-conductivity are in the orders of 0.1.

Such variance causes the resolution of an inverse problem in terms of constant bulk water content, expressed in log weight percentages, to be in the order of $0.1\ \log_{10}(wt\%)^2$. On the other hand such large posterior variance of the water content are much smaller than the differences between the upper and lower water content estimates in terms of the HS bounds.

When considering the full forward problem mapping upper mantle water content to the magnetic response to the M2 tidal forcing, the variances of the SH coefficient of the internal magnetic field are in the orders of $1\,\mu\mathrm{T}^2$.

This implies that such errors can pose a problem moving forward, although they do not blur the lines between the upper and lower water content estimates.

The lab-based conductivities and from them calculated synthetic conductivity of upper mantle do not account for the effect of possible errors introduced in the thermodynamic model and the possible inconsistency between the thermodynamically computed ideal phases and the in situ synthesized samples. This means that this work presents a lower error estimate for the methods presented above.

Bibliography

P. Alken, E. Thébault, C. D. Beggan, H. Amit, J. Aubert, J. Baerenzung, T. N. Bondar, W. J. Brown, S. Califf, A. Chambodut, A. Chulliat, G. A. Cox, C. C. Finlay, A. Fournier, N. Gillet, A. Grayver, M. D. Hammer, M. Holschneider, L. Huder, G. Hulot, T. Jager, C. Kloss, M. Korte, W. Kuang, A. Kuvshinov, B. Langlais, J. M. Léger, V. Lesur, P. W. Livermore, F. J. Lowes, S. Macmillan, W. Magnes, M. Mandea, S. Marsal, J. Matzka, M. C. Metman, T. Minami, A. Morschhauser, J. E. Mound, M. Nair, S. Nakano, N. Olsen, F. J. Pavón-Carrasco, V. G. Petrov, G. Ropp, M. Rother, T. J. Sabaka, S. Sanchez, D. Saturnino, N. R. Schnepf, X. Shen, C. Stolle, A. Tangborn, L. Tøffner-Clausen, H. Toh, J. M. Torta, J. Varner, F. Vervelidou, P. Vigneron, I. Wardinski, J. Wicht, A. Woods, Y. Yang, Z. Zeren, and B. Zhou. International geomagnetic reference field: the thirteenth generation. *Earth, Planets and Space*, 73(1):49, 2021. doi: 10.1186/s40623-020-01288-x. URL `https://doi.org/10.1186/s40623-020-01288-x`.

J. A. D. Connolly. The geodynamic equation of state: What and how. *Geochemistry, Geophysics, Geosystems*, 10(10), 2009. doi: https://doi.org/10.1029/2009GC002540. URL `https://agupubs.onlinelibrary.wiley.com/doi/abs/10.1029/2009GC002540`.

J.A.D. Connolly. Multivariable phase diagrams: an algorithm based on generalized thermodynamics. *American Journal of Science*, 290(6):666–718, 1990. ISSN 00029599. URL `https://search.ebscohost.com/login.aspx?authtype=shib&custid=s1240919&profile=eds`.

J.A.D. Connolly. Computation of phase equilibria by linear programming: A tool for geodynamic modeling and its application to subduction zone decarbonation. *Earth and Planetary Science Letters*, 236(1):524–541, 2005. ISSN 0012-821X. doi: https://doi.org/10.1016/j.epsl.2005.04.033. URL `https://www.sciencedirect.com/science/article/pii/S0012821X05002839`.

Lidong Dai and S. Karato. Electrical conductivity of pyrope-rich garnet at high temperature and high pressure. 176(1):83–88, 2009. ISSN 0031-9201. doi: https://doi.org/10.1016/j.pepi.2009.04.002. URL `https://www.sciencedirect.com/science/article/pii/S0031920109000685`.

Sylvie Demouchy, Svyatoslav Shcheka, Carole M. M. Denis, and Catherine Thoraval. Subsolidus hydrogen partitioning between nominally anhydrous minerals in garnet-bearing peridotite. 102(9):1822–1831, 2017. ISSN 0003-004X.

A.M. Dziewonski and D.L. Anderson. Preliminary reference earth model. *Phys. Earth Plan. Int.*, pages 297–356, 1981. doi: 10.17611/DP/9991844.

Gary D. Egbert and Svetlana Y. Erofeeva. Efficient inverse modeling of barotropic ocean tides. *Journal of Atmospheric and Oceanic Technology*, 19 (2):183 – 204, 2002. doi: 10.1175/1520-0426(2002)019⟨0183:EIMOBO⟩2.0.CO;2. URL `https://journals.ametsoc.org/view/journals/atot/19/2/1520-0426_2002_019_0183_eimobo_2_0_co_2.xml`.

David Einšpigel and Zdeněk Martinec. Time-domain modeling of global ocean tides generated by the full lunisolar potential. *Ocean Dynamics*, 67(2):165–189, 2017. doi: 10.1007/s10236-016-1016-1. URL https://doi.org/10.1007/s10236-016-1016-1.

J Fullea, S Lebedev, Z Martinec, and N L Celli. WINTERC-G: mapping the upper mantle thermochemical heterogeneity from coupled geophysical–petrological inversion of seismic waveforms, heat flow, surface elevation and gravity satellite data. *Geophysical Journal International*, 226(1):146–191, 03 2021. ISSN 0956-540X. doi: 10.1093/gji/ggab094. URL https://doi.org/10.1093/gji/ggab094.

Alexander V. Grayver and Nils Olsen. The magnetic signatures of the m2, n2, and o1 oceanic tides observed in swarm and champ satellite magnetic data. *Geophysical Research Letters*, 46(8):4230–4238, 2019. doi: https://doi.org/10.1029/2019GL082400. URL https://agupubs.onlinelibrary.wiley.com/doi/abs/10.1029/2019GL082400.

Amir Khan. On earth's mantle constitution and structure from joint analysis of geophysical and laboratory-based data: An example. *Surveys in Geophysics*, 37(1):149–189, Jan 2016. ISSN 1573-0956. doi: 10.1007/s10712-015-9353-z. URL https://doi.org/10.1007/s10712-015-9353-z.

Ondřej Knopp. Electrical conductivity of the mantle and its thermochemical and mineralogical state: Forward problem. *Bachelor thesis, Charles University, Faculty of Mathematics and Physics*, 2021.

Zdeněk Martinec. Spectral-finite element approach to three-dimensional electromagnetic induction in a spherical earth. *Geophysical Journal International*, 136 (1):229–250, 01 1999. ISSN 0956-540X. doi: 10.1046/j.1365-246X.1999.00713.x. URL https://doi.org/10.1046/j.1365-246X.1999.00713.x.

Zdeněk Martinec, Javier Fullea, Jakub Velímský, and Libor Šachl. A new integrated geophysical-petrological global 3-D model of upper-mantle electrical conductivity validated by the Swarm M2 tidal magnetic field. *Geophysical Journal International*, 226(2):742–763, 04 2021. ISSN 0956-540X. doi: 10.1093/gji/ggab130. URL https://doi.org/10.1093/gji/ggab130.

Davide Novella, Daniel J. Frost, Erik H. Hauri, Helene Bureau, Caroline Raepsaet, and Mathilde Roberge. The distribution of h_2o between silicate melt and nominally anhydrous peridotite and the onset of hydrous melting in the deep upper mantle. *Earth and Planetary Science Letters*, 400:1–13, 2014. ISSN 0012821X. doi: 10.1016/j.epsl.2014.05.006.

Terence J. Sabaka, Robert H. Tyler, and Nils Olsen. Extracting ocean-generated tidal magnetic signals from swarm data through satellite gradiometry. *Geophysical Research Letters*, 43(7):3237–3245, 2016. doi: https://doi.org/10.1002/2016GL068180. URL https://agupubs.onlinelibrary.wiley.com/doi/abs/10.1002/2016GL068180.

Terence J. Sabaka, Lars Tøffner-Clausen, Nils Olsen, and Christopher C. Finlay. Cm6: a comprehensive geomagnetic field model derived from both champ and swarm satellite observations. *Earth, Planets and Space*, 72(1):80, 2020. doi: 10.1186/s40623-020-01210-5. URL https://doi.org/10.1186/s40623-020-01210-5.

Lars Stixrude and Carolina Lithgow-Bertelloni. Mineralogy and elasticity of the oceanic upper mantle: Origin of the low-velocity zone. *Journal of Geophysical Research: Solid Earth*, 110(B3), 2005a. doi: https://doi.org/10.1029/2004JB002965. URL https://agupubs.onlinelibrary.wiley.com/doi/abs/10.1029/2004JB002965.

Lars Stixrude and Carolina Lithgow-Bertelloni. Thermodynamics of mantle minerals — I. Physical properties. *Geophysical Journal International*, 162(2):610–632, 08 2005b. ISSN 0956-540X. doi: 10.1111/j.1365-246X.2005.02642.x. URL https://doi.org/10.1111/j.1365-246X.2005.02642.x.

Lars Stixrude and Carolina Lithgow-Bertelloni. Influence of phase transformations on lateral heterogeneity and dynamics in earth's mantle. *Earth and Planetary Science Letters*, 263(1):45–55, 2007. ISSN 0012-821X. doi: https://doi.org/10.1016/j.epsl.2007.08.027. URL https://www.sciencedirect.com/science/article/pii/S0012821X07005377.

Albert Tarantola. *Inverse Problem Theory and Methods for Model Parameter Estimation*. Society for Industrial and Applied Mathematics, 2005. doi: 10.1137/1.9780898717921. URL https://epubs.siam.org/doi/abs/10.1137/1.9780898717921.

Georgios P. Triberis. *Small Polaron Hopping DC Conductivity in 3D and 1D Disordered Materials.* Materials Science and Technologies. Nova Science Publishers, Inc, 2017. ISBN 9781536119435. URL https://search.ebscohost.com/login.aspx?authtype=shib&custid=s1240919&profile=eds.

Jakub Velímský, Alexander Grayver, Alexey Kuvshinov, and Libor Šachl. On the modelling of M_2 tidal magnetic signatures: Effects of physical approximations and numerical resolution. 70:192, 2018. doi: 10.1186/s40623-018-0967-5.

Jakub Velímský and Zdeněk Martinec. Time-domain, spherical harmonic-finite element approach to transient three-dimensional geomagnetic induction in a spherical heterogeneous Earth. *Geophysical Journal International*, 161(1):81–101, 04 2005. ISSN 0956-540X. doi: 10.1111/j.1365-246X.2005.02546.x. URL https://doi.org/10.1111/j.1365-246X.2005.02546.x.

Wenbo Xu, Carolina Lithgow-Bertelloni, Lars Stixrude, and Jeroen Ritsema. The effect of bulk composition and temperature on mantle seismic structure. *Earth and Planetary Science Letters*, 275(1):70–79, 2008. ISSN 0012-821X. doi: https://doi.org/10.1016/j.epsl.2008.08.012. URL https://www.sciencedirect.com/science/article/pii/S0012821X08005281.

Yousheng Xu, Shun-ichiro Karato, Duojun Wang, and Mainak Mookherjee. The effect of water on the electrical conductivity of olivine. *Nature*, 443(7114):977–980, 2006. ISSN 0028-0836.

Takashi Yoshino. Laboratory electrical conductivity measurement of mantle minerals. *Surveys in Geophysics*, 31(2):163–206, Mar 2010. ISSN 1573-0956. doi: 10.1007/s10712-009-9084-0. URL https://doi.org/10.1007/s10712-009-9084-0.

Baohua Zhang, Takashi Yoshino, Wu Xiaoping, Takuya Matsuzaki, Shuangming Shan, and Tomoo Katsura. Electrical conductivity of enstatite as a function of water content; implications for the electrical structure in the upper mantle. 357-358:11–20, 2012. ISSN 0012-821X.

Chengcheng Zhao and Takashi Yoshino. Electrical conductivity of mantle clinopyroxene as a function of water content and its implication on electrical structure of uppermost mantle. 447:1–9, 2016. ISSN 0012-821X.

L Šachl, J Velímský, J Fullea, and Z Martinec. Inversion of the satellite observations of the tidally induced magnetic field in terms of 3-D upper-mantle electrical conductivity: method and synthetic tests. *Geophysical Journal International*, 229(3):2115–2132, 01 2022. ISSN 0956-540X. doi: 10.1093/gji/ggac015. URL https://doi.org/10.1093/gji/ggac015.

L Šachl, O Knopp, and J Velímský. Electrical conductivity of the suboceanic upper mantle constrained by satellite-derived tidal magnetic fields: 3-d inversion, validation and interpretation. *Geophysical journal international*, pages 1254–1268, 2024. ISSN 0956-540X. doi: https://doi.org/10.1093/gji/ggae209.

List of Figures

List of Tables